Journal of Molecular Structure 1286 (2023) 135569

Contents lists available at ScienceDirect

Journal of Molecular Structure

journal homepage: www.elsevier.com/locate/molstr

# Synthesis, Crystal structure, Hirshfeld surface interactions, anti-corrosion analysis, DFT calculations, Docking studies and evaluation of the antioxidant activity of a new zwitterion Schiff base

Redouane Lemoui [a,b], Hamza Allal [c,d], Douniazed Hannachi [e,f], Amel Djedouani [b,g], Imen Ramli [h,i], Said Mohamed el hadi [c], Imane Habila [c], Mohamed Zabat [j], Hocine Merazig [c], Helen Stoeckli-Evans [g], Nadir Ghichi [c,*]

[a] Unit for Valorization of Natural Resources, Bioactive Molecules and Physicochemical and Biological Analyzes (VARENBIOMOL), University of the Brothers Mentouri Constantine, Constantine, Algeria
[b] Ecole Normale Supérieure Assia Djebar of Constantine, Department of Physics and Chemistry, University Constantine 3, 250 0 0, Algeria
[c] Unit of Research CHEMS, Chemistry Department, University of Mentouri Brothers, Constantine 1, Algeria
[d] Department of Process Engineering, Faculty of Process Engineering, Salah Boubnider Constantine 3 University, Constantine, Algeria
[e] Laboratory of Electrochemistry, Molecular Engineering and Redox Catalysis (LEIMCR), Department of Basic Education in Technology, Faculty of Technology, Ferhat Abbas University, Sétif-1, Algeria
[f] Department of Chemistry, Faculty of Sciences, University of Setif-1, Setif, Algeria
[g] Laboratory of Analytical Physicochemistry and Crystallochemistry of Organometallic and Biomolecular Materials, University Constantine 1, 250 0 0, Algeria
[h] Laboratory of ethnobtany palynology and ethno-pharmacology and toxicology (LEPET)
[i] Laboratory for obtaining therapeutic substances (LOST)jLaboratory of Natural Products of Plant Origin and Organic Synthesis, University of the Mentouri Brothers, Constantine, 25000, Algeria
[j] Institute of Physics, University of Neuchâtel, 2000, Neuchâtel, Switzerland

ARTICLE INFO

*Keywords:*
X-ray, Schiff base, HS, Antioxidant activity, Molecular docking
Anti-corrosion, DFT-TD-DFT calculations

ABSTRACT

The title compound Schiff base (**SB**) named: (6E)-3-benzyloxy-6- [ [ [2-hydroxy-1,1-bis(hydroxymethyl)ethyl] amino]methylene]cyclohexa-2,4-dien-1-one(**I**) ($C_{18}$ $H_{21}$ N $O_5$), was synthesized via the reaction of 4-benzyloxy-2-hydroxy-benzaldehyde with 2-amino-2-(hydroxymethyl)propane-1,3-diol (Trizma)and characterized by single-crystal diffraction XRD, infrared spectra, $^{1}$H and $^{13}$C NMR spectroscopy. It crystallizes as a zwitterion, (*E*)-5-(benzyloxy)-2-(((1,3-dihydroxy-2-(hydroxymethyl)propan-2-yl)iminio)methyl)phenolate **(II),** with the phenolic H atom having migrated to the imino group. Additionally,Hirshfeld surface analysis (HS), two-dimensional fingerprint plots and energy frameworks of **II** were calculated to quantify the interatomic interactions present in the crystal.The antioxidant activity of the synthesized compound was evaluated by five tests: ABTS, DPPH, O-pH, SNP and reducing power activity. Furthermore, molecular docking calculations were performed for SB compound at the active site of mushroom tyrosinase (PDB ID:2Y9X) to determine the binding affinity between the title compound and receptor protein. Results reveal a great affinity (-6.16 kcal/mol) of the SB to the protein that is mainly dominated by hydrogen bonds. In this work, experimentally, the assessment of the anti-corrosion ability of this compound by different methods showed excellent inhibition. On the other hand, anti-corrosion potentials of title compound have been investigated using density functional theory (DFT) in gas and solvent phases. Chemical reactivity descriptors like global hardness (η), chemical potential (u), electronegativity (χ), electrophilicity (ω) and number of transferred electrons (ΔN) were computed at ωB97XD with 6–311+*g*(d) basis set. The local reactive sites on this compound were studied using Fukui indices, local philicity index and dual descriptor. The quantum chemical calculation suggests a good charge transfer tendency from the title compound to the low-lying vacant d-orbitals of iron (The average value of charge transfer is $\Delta N_{III/Fe}$.≈ 2.21 and $\Delta N_{III/Cu}$.≈ 0.07). The C7 atom is the nucleophilic sites ($\Delta f(r)_{C7} \approx 0.25$) on the inhibitor for effective interaction on the metal surface as shown by local reactive descriptor in gas and solvent. Furthermore, the results obtained from DFT and TD-DFT studies are in excellent agreement with experimental data (structure geometry (RMS Error ≈ 0.3 Å), optical properties ($\lambda_{exp\text{-}Cal}$ ≈18 nm) and inhibition efficiencies).

* Corresponding author.
*E-mail address:* nadirgh82@hotmail.com (N. Ghichi).

https://doi.org/10.1016/j.molstruc.2023.135569
Received 14 January 2023; Received in revised form 28 March 2023; Accepted 11 April 2023
Available online 14 April 2023

## 1. Introduction

Schiff base ligands (also known as imine or azomethine) are the compounds containing azomethine group (-HC═N-) and they play an important role as chelating ligands in both main group metal and transition metal coordination chemistry [1]. They were first reported by Hugo Schiff in 1864 [2] and considered "privileged ligands'' [3] because they are easily prepared by combining a primary amine and an aldehyde or a ketone under specific conditions.

Structurally talking, a Schiff base is a nitrogen analog of an aldehyde or ketone in which the carbonyl group (CO) has been replaced by an imine or azomethine group [4] and they are formed more readily with aldehydes than with ketone. Schiff base ligands have significant importance in chemistry and appear to be an important intermediate in a number of enzymatic reactions involving the interaction of an enzyme with an amino or a carbonyl group of the substrate [3]. There have been many reports on their applications in biology including antibacterial, antifungal, anticancer, antioxidant, anti-inflammatory activity and as catalysts in several reactions [4]. Aromatic aldehydes especially with an effective conjugation system, form stable Schiff bases, whereas those aliphatic aldehydes are unstable and facilely polymerize. [2]. A wide range of Schiff base compounds are broadly studied due to their flexible and diverse structure. Their containment of the azomethine functional group imparts to them great flexibility and structural diversity [4]. Therefore, researchers study the physical and chemical properties of these compounds to better understand their behavior and potential applications in various fields such as catalysis, organic synthesis, and materials science [5]. Their chemical and physical properties in various field such as identification, protection and determination of aldehyde or ketones, purification of carbonyl and amino compounds and production of these compounds in complex have been worked on by various workers [6].

Recently, some ortho-hydroxyamino derivatives have been synthesized and found to possess enhanced antioxidant activity. These derivatives are organic compounds that contain both a hydroxyl (-OH) and an amino (-NH2) functional group attached to the ortho position (immediately adjacent) of an aromatic ring. The synthesis and evaluation of these derivatives for their antioxidant activity can provide insights into the relationship between their chemical structure and biological properties. The enhanced antioxidant activity of these derivatives suggests their potential application in medicinal chemistry for developing new therapeutic agents. [7]. Their Schiff bases belongs to a class of compounds with very short and strong hydrogen bonds, which is formed between the nitrogen atom of the Schiff base moiety and the hydroxyl group from the ortho position of the aromatic ring [8].These intramolecular hydrogen bridges are of significant interest to researchers, and as such, they are extensively studied using diffractometry and spectroscopic techniques such as NMR and IR. The use of diffractometry and spectroscopy helps researchers gaina better understanding of these bonds and explore potential applications in various fields, such as materials science and drug discovery [9–11].

Tris(hydroxymethyl)aminomethane (TRIS) is a chemical compound with a tertiary amine and is widely used to maintain the pH of solutions within a certain range, especially for biological applications. It is considered to be an effective buffer because its pKa value is close to the physiological pH range, also, the literature mentions that (TRIS) and its Schiff base derivatives are known to have a broad spectrum of biological activities such as anti-tumor, antibiotic, anticancer, antifungal, anti-inflammatory and many others [12,13]. Additionally, TRIS is known to participate in enzymatic reactions by forming compounds with carbonyl substrates and act as a catalyst. This versatility and usefulness make it a vital tool in biochemical research, medical diagnosis, and treatment [14].

For this purpose, a new Schiff base ligand was synthesized successfully. We using a conventional soft chemistry-based route by the reaction of an aromatic aldehyde and TRIS organic ligand. We report in the current article the synthesis, structure interpretation, corrosion inhibitory and biological activities of this new compound, **(*E*)−2-((4-(benzyloxy)−2-hydroxybenzylidene)amino)2-(hydroxymethyl) propane-1,3-diol (I)**. Quantum chemical calculation by using a Density Functional Theory (DFT) is considered to be an efficient and accurate method of predicting, designing and investigating the corrosion inhibition potentials of compounds. On the other hand, the DFT method provides insight into the reactivity parameters (local and global) of molecules and the relationship between these parameters and corrosion inhibition efficiency. Therefore, detailed quantum chemical calculation have been performed to investigate the corrosion inhibition potential of title compound via DFT method. Geometry parameters, reactivity descriptors, optical proprietis and interactions of (E)−2-((4-(benzyloxy)−2-hydroxybenzylidene)amino)−2-(hydroxymethyl)propane-1,3-diol on iron and copper surfaces in gas and solvents were studied using DFT and TDDFT. Moreover, molecular docking studies were also performed to identify the interactions between the title compound and the active site of the mushroom tyrosinase (PDB ID 2Y9X), in order to evaluate its potential biological significance as an antioxidant agent.

## 2. Experimental

### 2.1. Measurements and materials

All reagents used for the (6E)−3-benzyloxy-6- [ [ [2-hydroxy-1,1-bis (hydroxymethyl) ethyl] amino] methylene]cyclohexa-2,4-dien-1-one (**I**) synthesis were used without further purification. The NMR spectra were recorded on a Bruker Avence DPX 250 MHz spectrometer 250 for $^{1}H$ and $^{13}C$. We recorded the IR spectrum in the range of (600 and 3500 $cm^{-1}$) and resolution of 4,0 $cm^{-1}$ using the Jasco spectrometer (FT/IR-6300). UV–visible Spectrometer Thermo Electron Corporation Model NICOLET evolution 300.

### 2.2. XRD and HSA computing details

Data collection: APEX2 [15]; cell refinement: SAINT [15]; data reduction: SAINT [15]; program(s) used to solve structure: SHELXT 2014/4 [16]; program(s) used to refine structure: SHELXL2018/3 [17]; molecular graphics: Mercury [18]; software used to prepare material for publication: PLATON [19], SHELXL2018/3 [17]. Crystal data, data collection and structure refinement details are summarized in Table 1 and selected geometric parameters are presented in Table 2 . The NH and $N^{+}$- H atoms were located in a difference-Fourier map and freely refined. The C-bound H atoms were positioned geometrically (C–*H* = 0.93–0.97 ˚A) and refined as riding with $U_{iso}(H) = 1.5\ U_{eq}$ (C). The Hirshfeld surface analysis [20] and the associated two-dimensional fingerprint plots [21] were performed with Crystal Explorer 21 [22] following the protocol of Tiekink and collaborators [23].

### 2.3. Computational details

The geometries of the title compound were fully optimized using the ωB97XD density functional [24,25] with 6–311+*g*(d) basis set [26,27]. The ωB97XD is a range-separated hybrid exchange-correlation functional that includes damped atom-atom dispersion corrections [24,28]. To include the solvent effects in the quantum calculations, we have employed the self-consistent reaction field (SCRF) approach with the polarizable continuum model (PCM). [29,30] No symmetry constraints were applied and the local minima on the potential energy surface were confirmed by harmonic frequency calculations of the ground state at the same levels of approximation. All geometric, optical and electronic parameters calculations in gas and solvent namely chloroform (ε=4.7113), methanol (ε=32.613), acetonitrile (ε=35.688) and water (ε=78.355) were performed using the Gaussian09 package.

The global chemical reactivity descriptors such as chemical hardness (η), electronic chemical potential (μ), electronegativity (χ) and global

**Table 1**
Crystallographic data and structure refinement parameters for II.

| CCDC Number | 2,233,190 |
|---|---|
| Chemical formula | $C_{18}$ $H_{21}$ N $O_5$ |
| Weight | 331.36 |
| Crystal color | Green |
| Crystal system | Orthorhombic |
| Space group | P b c a |
| *a (Å)* | 9.263(1) |
| *b (Å)* | 9.2631(11) |
| *c (Å)* | 38.528(5) |
| Volume ($Å^3$): | 3305.9(6) |
| T (K) | 293 |
| Radiation Type | Mo\Kα |
| Z | 8 |
| μ ($mm^{-1}$) | 0.097 |
| Reflections measured | 15,725 |
| Reflections independent | 4545 |
| $R_{int}$ | 0.079 |
| Data/parameters/restraints | 4545/233/0 |
| Final R indexes [$F^2$>2σ($F^2$)] | R1 = 0.048, w$R(F^2)$ = 0.109 |
| Goodness of Fit on $F^2$ | 0.832 |
| $\Delta\rho_{max}/\Delta\rho_{min}$ (e $Å^{-3}$) | 0.18/−0.18 |

**Table 2**
Selected bond distances (Å) and bond angles (°) for II.

| Bond lengths (Å) | | Bond Angle(°) | |
|---|---|---|---|
| O1—C7 | 1.281(2) | C5—O2—C8 | 117.82 (14) |
| O2—C5 | 1.3674 (17) | O2—C8—C9 | 107.70 (14) |
| O2—C8 | 1.4272 (18) | C1—N1—C15 | 127.12 (12) |
| O3—C16 | 1.428(2) | N1—C1—C2 | 125.16 (14) |
| O4—C17 | 1.4161 (18) | O2—C5—C6 | 125.23 (13) |
| O5—C18 | 1.4287 (19) | O2—C5—C4 | 112.96 (15) |
| N1—C1 | 1.291 (2) | O1—C7—C2 | 120.56 (13) |
| N1—C15 | 1.4799 (17) | O1—C7—C6 | 122.87 (14) |
| C1—C2 | 1.4096(19) | O5—C18—C15 | 114.91 (13) |
| C15—C16 | 1.529(2) | N1—C15—C17 | 106.68 (12) |
| | | N1—C15—C16 | 105.44 (10) |
| | | N1—C15—C18 | 112.28 (13) |
| | | O3—C16—C15 | 108.97 (13) |
| | | O4—C17—C15 | 108.94 (12) |

electrophilicity index were evaluated from the frontier orbital energies HOMO and LUMO ($\varepsilon_H$ and $\varepsilon_L$, respectively) by the following equation: [31,32]

$$\mu = \frac{1}{2}(\varepsilon_H + \varepsilon_L) = -x \quad (1)$$

$$\varepsilon_L - \varepsilon_H \quad (2)$$

$$\omega = \frac{\mu^2}{2} \quad (3)$$

The chemical potential (μ) characterizes the escaping tendency of electrons from the equilibrium system. The chemical hardness (η) measures the stability of a compound in terms of resistance to electron transfer. The global electrophilicity index (ω), introduced by Parr et al. [32], for expresses the ability of a molecule to accept electrons from the environment.

During the interaction between the inhibitor molecule and metal, the electrons flow from the lower electronegativity molecule (nucleophile, Nu) to the higher electronegativity metal (electrophile, E) until the chemical potential becomes equalized. The fraction of the transferred electron, Δ*N*, was estimated according to Pearson.

$$\Delta N = \frac{\mu_{Nu} - \mu_E}{2(\eta_{Nu} + \eta_E)} \quad (4)$$

On the other hand, the Fukui function $f(r)$ is local reactivity descriptor reflects the ability of a molecular site to donate or accept the electrons. Gázquez and Méndez demonstrated that sites in chemical species with the high values of $f(r)$are related to a high reactivity at point r [33,34]. The Fukui function for an atom k in a molecule can be expressed as:

$$f_k^- - = q_k(N) - q_k(N-1) \Rightarrow forelectrophilicattack \quad (5)$$

$$f_k^+ = q_k(N+1) - q_k(N) \Rightarrow fornucleophilicattack \quad (6)$$

Where, $q_k$ is the atomic charge at the k atomic site in the neutral (N), anionic ($N+1$) and cationic (N-1) chemical species (N is the number of electrons).

Furthermore, the local philicity index ($\omega_k^\alpha$) can easily be evaluated from these equations [35,36]:

$$\omega_k^\alpha = \omega f_k^\alpha \quad (7)$$

Where, α= + or - refer to nucleophilic and electrophilic attacks, respectively.

The dual descriptor developed by Morell et al. [37,38] is a useful function used also to reveal the local reactivity sites of compounds. It can be approximated by:

$$\Delta f(r) \approx \rho_{N+1}(r) + \rho_{N-1}(r) - 2\rho_N(r) \quad (8)$$

The sign of dual descriptor is an important criterion of reactivity site within a molecule.

Ø If $\Delta f(r) > 0$, then the site is favorable for a nucleophilic attack.
Ø If $\Delta f(r) < 0$, then the site is favorable for an electrophile attack.

### 2.4. Anti-corrosion details

#### 2.4.1. Preparation of corrosive solution

The studied corrosion solution is 0.5 M $H_2SO_4$ diluted from 98% concentrated acid, with different concentrations of inhibitors.

#### 2.4.2. Inhibitors

The structure of the studied inhibitor, compound (**I**), is shown in the Scheme 1.

#### 2.4.3. Mild steel specimen

The working electrode is made of steel (API5L grade B) coated with epoxy resins and have an exposed area of 0.34 $cm^2$. Was polished with abrasive papers of different grades (400, 800, 1200, and 2000 grit), rinsed, and degreased with ethanol, rinsed several times with distilled water, and then drying before measurement.

A conventional three-electrode cylindrical glass cell was used for both potentiodynamic polarization analysis and electrochemical impedance spectroscopy. Electrodes used for electrochemical measurements are a platinum electrode as the counter electrode and a saturated calomel electrode as a reference electrode. Polarization and impedance measurements were performed using a potentiostat/ galvanostat/ZRA « GAMRY-Reference 3000». Potentiodynamic polarization experiments were performed in the potential range of −800 to -200 mV using a scan rate of 1 mV.$s^{-1}$. Inhibition efficiency (*IE*%) values are obtained in this method using the following equation 1:

$$IE(\%) = \frac{I_{corr(0)} - I_{corr(h)}}{I_{corr(0)}} \times 100 \quad (9)$$

$I_{corr}$ and $I_{corr,0}$ are the current densities in the presence or absence of the investigated inhibitors, respectively.

Electrochemical impedance spectroscopy (EIS) was performed at open circuit potential ($E_{corr}$) over a frequency range of 100 kHz-10 mHz with a 10 mV peak-to-peak amplitude using the AC signal. Here the inhibition efficiency (IE%) is calculated starting from the charge transfer resistance, as in the following Eq. (2).

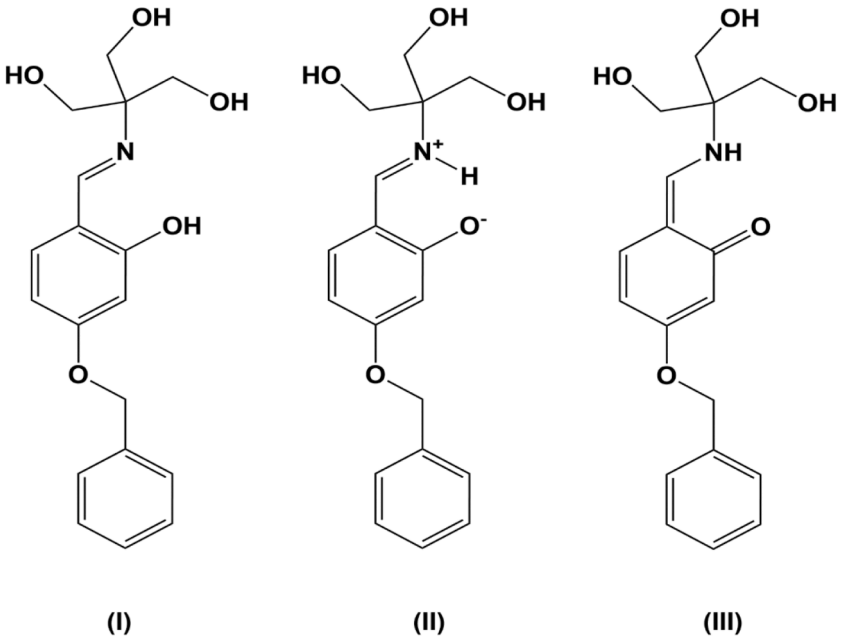


**Scheme 1.**

$$IE(\%) = \frac{R_{ct(h)} - R_{ct(0)}}{R_{ct(h)}} \times 100 \quad (10)$$

### 2.5. Antioxidant activity

#### 2.5.1. ABTS radical cation scavenging activity

The antioxidant activity of our compound was assessed using the ABTS radical cation scavenging activity according to the method developed by *Re* et al. [14] based on the reduction of ferric iron ($Fe^{3+}$) in the K3Fe (CN)6 complex to ferrous iron ($Fe^{2+}$) solution. Briefly, ABTS solution (2,2′-azino-bis (3-ethylbenzothiazoline-6-sulfonic acid) ($ABTS^{\bullet+}$) 19.2 mg (7 mM) was added to a potassium persulfate (2.45 mM) solution and incubated for 12-16 h in the dark to yield a blue-green colored solution containing ABTS radical cation. Then, the absorbance of the resulting blue-green $ABTS^{+\bullet}$ solution was adjusted to an initial absorbance of about 0.700 ± 0.02 at 734 nm. Then 40 µl of the tested sample was mixed with 160 µl of ABTS radical solution and the absorbance was measured after 10 min at 734 nm. The antioxidant capacity of the test sample was expressed as $IC_{50}$, the concentration necessary for a 50% reduction of ABTS cation. Butylated hydroxyanisole (BHA), butylated hydroxytoluene (BHT), Ascorbic acid and Trolox (6-hydroxy-2,5,7,8-tetramethylchroman-2-carboxylic acid) were used as reference standards.

#### 2.5.2. DPPH radical scavenging assay

The free radical scavenging activity was measured according to the DPPH method described by Blois et al. [39]. Briefly, 160 µL of DPPH (2, 2-diphenyl-1-picryl-hydrazine-hydrate) solution (60 µM) was added to 40 µL of different extract concentrations and then incubated for 30 min. The scavenging capacity was measured using a 96 microplate spectrophotometer reader and the absorbance was measured at 517 nm. The results were expressed as the inhibitory concentration of 50% of free radicals (µg/mL).

#### 2.5.3. O-Phenanthroline free radical reducing activity

This assay was performed according to Szydłowska-Czerniak et al. [40] method. A mixture of 30 µL of O-phenanthroline (0.5%), 50µL $FeCl_3$ (0.2%), 110 µL Methanol. This mixture was added to 10 µL of different concentrations of plant extract and incubated for 20 min at 30 °C. Then the absorbance was measured at 510 nm. The results were expressed as the percentage of inhibition.

#### 2.5.4. Silver nanoparticle assay (SNP)

Silver ions (Ag+) reduction was evaluated as described by Ozyurek et al. [41] method. Briefly, 50 ml of distilled water and 130 mL of SNP solution (1 mM AgNO3, 1% citrate solution) were added to 20 ml of the studied compound or standard molecules in a microplate. The mixture was incubated at 25 °C for 30 min, then the absorbance was measured at 423 nm, and A0.5 were determined from the regression curves.

#### 2.5.5. Reducing power

The capacity of the compound reduce iron ions ($Fe^{3+}$) was determined as described by Oyaizu [42] (1986) with slight modifications. Briefly, 10 µL of our sample at different concentrations was mixed with 40 µL of phosphate buffer (0.2 M, pH 6.6) and 50 µL of 1% potassium ferricyanide solution. The mixture was then incubated in an oven at 50 °C for 20 min. Then, 50 µL of 10% tri-chloroacetic acid, 40 µL of distilled water, and 10 µL of 0.1%ferric chloride ($FeCl_3$) solution were added. The absorbance was directly read at 700 nm using a microplate reader (Perkin Elmer, Enspire, Singapore). The results were compared to the standard BHA $A_{0.5}$ corresponding to the concentration of the sample giving an absorbance of 0.5 and the absorbance curve was plotted with different concentrations.

### 2.6. Molecular docking

Molecular docking studies were carried out using AutoGrid and AutoDock executable programs implemented in MGLtools (AutoDock Tools) [43]. The 3D crystal of the tyrosinase (PDB ID: 2Y9X) [44] was downloaded from the protein data bank (PDB) https://www.rcsb.org/structure/2Y9X. For the preparation of receptor, all chains (except chain A), ligands, ions and water molecules were removed, then non-polar hydrogens were merged and Kollman partial charges were added. Docking studies were analysed using the Lamarckian genetic algorithm (LGA) [43]. The 3D grid size was set to 80 × 80 × 80 points with a grid spacing of 0.375 Å. Among the all docked results, only the best pose (with the lowest binding energy) was selected and considered with a root-mean-square deviation of less than 1 Å. The best protein–ligand pose was visualized by Chimera software (version 1.10.2) [45] and Discovery Studio Visualization BIOVIA (version 20.1) [46].

### 2.7. Synthesis and crystallization

A mixture of 4-benzyloxy-2-hydroxy-benzaldehyde (1 equiv.) with 2-amino-2-(hydroxymethyl)propane-1,3-diol (1 equiv.), was stirred for sufficient time. The solvent Methanol was evaporated in vacuo andthe residue yielded green block-like crystals on slow evaporation of the solvent. X-ray diffraction analysis indicated that in the solid state the compound exists as the Zwitterion (*E*)−5-(benzyloxy)−2-(((1,3-dihydroxy-2-(hydroxymethyl)propan-2-yl)iminio) methyl) phenolate (**II**), see Scheme .IR($\upsilon$/cm$^{-1}$), 2368,07(b); 1500(e). $^{1}$H NMR (250 MHz, $CDCl_3$), $\delta$ ppm: 8.2 (s, 1H, CH═N); 14.1 (s, 1H, $OH_{ar}$); 3.4 (s, 2H, $CH_2$); 3.6 (s, 2H, $CH_2$); 4.9 (s, 2H, $CH_2$); 5.1 (s, 2H, $OCH_2$); 7–7.3 (m, 8H, $H_{ar}$) The $^{13}$C NMR, 162.08 (CH═N); 163.88 (C—OH); 127.72–136.86 (C = C ar); 69.00 ($CH_2$—O).

## 3. Results and discussions

### 3.1. Analytical data

#### 3.1.1. FT-IR spectroscopy

The analysis of the IR experimental spectrum of compound (**I**) shows the presence of the following characteristic peaks Fig. 1: The bands observed around 2368,07cm$^{-1}$ are assigned to C—H bending (aromatic compound). The spectra show a broad absorption band at (2924,56 3347,23cm$^{-1}$) due to the stretching elongation vibration of the C–H aromatic and of the C–H aliphatic, respectively. The peak with average intensities obtained about 1500 cm$^{-1}$ can be referred to the C = C aromatic elongation. Hence, the IR spectra of **I**, agrees with the structure determined by the X-ray diffraction analysis.

#### 3.1.2. $^{1}$H NMR spectroscopy

The $^{1}$H NMR spectroscopic analysis confirms the proposed structure of the title compound. Proton H1 of atom the carbone C1 and imine fonction appears at 8.2 ppm (s, 1H, CH). A multiplet between 7–7.3 ppm corresponds to protons H aromatics (m, 8H, H-ar). The singlet between (3.4–5.1) corresponds to protons H ($CH_2$) (s,8H,$CH_2$).

#### 3.1.3. $^{13}$C NMR spectroscopy

The $^{13C}$ NMR spectra of the title compound allowed us to identify the characteristic carbons. The group of the CH═N fonction appear at 162.08 ppm and the aromatics carbons C = C appear between 127.72–136.86. The group of $CH_2$—O presented at 69.00 ppm.

### 3.2. Structural commentary and supramolecular features

The crystals of compound (**I**) were obtained by slow evaporation of a solution in ethanol. The main crystal parameters are reported in Table 1. Selected bond distances and angles are listed in Table 2. The numbering scheme and a displacement ellipsoid plot is shown in Fig. 2. Compound (**I**) crystallized in the orthorhombic crystal system, space group in Pbca and with eight molecules per unit cell ($Z$ = 8). It crystallizes as a zwitterion, **(*E*)−5-(benzyloxy)−2-(((1,3-dihydroxy-2-(hydroxymethyl) propan-2-yl)iminio)methyl)phenolate (II)**, with the phenolic H atom having been transferred to the imino group. The resulting iminio and phenolate groups are linked by an intramolecular charge assisted $N^{+}$—H···$O^{-}$ hydrogen bond, enclosing an S(6) ring motif. The configuration about the C = N bond is *E* and the dihedral angle between the two aromatic rings (C2-C7 and C9-C14) is 75.44(9)°.

In the crystal, molecules are aligned head-to-head/tail-to-tail in a *zigzag* fashion along *c*-axis direction Fig. 3. The molecules are linked *via* O—H···O hydrogen bonds Fig. 4 and Table 3, forming slabs lying parallel to the *ab*-plane Fig. 4.

#### 3.2.1. Hirshfeld surface analysis and two-dimensional fingerprint plots for II

The Hirshfeld surface analysis [20] and the associated two-dimensional fingerprint plots [21] were performed with CrystalExplorer17 [22] following the protocol of Tiekink and collaborators [23] (Tan et al., 2019). The Hirshfeld surface is color-mapped with the normalized contact distance, $d_{norm}$, from red (distances shorter than the sum of the van der Waals radii) through white to blue (distances longer than the sum of the van der Waals radii). The Hirshfeld surfaces of **II** mapped over $d_{norm}$, is given in Fig. 5*a*. The large red spots indicate that short contacts are significant in the crystal packing of both compounds.

The full two-dimensional fingerprint plots for **II** are given in Fig. 5*b*. The H···H contacts have a major contribution of 49.8% to the Hirshfeld surface (HS), while the C···H/H···C contacts contribute 26.7%. The O···H/H···O contacts contribute 22.8%, with extremely sharp spikes at $d_i + d_e \sim 1.6$ Å.

#### 3.2.2. Energy frameworks for II

The color-coded interaction mappings within a radius of 6 Å of a central reference molecule for **II**, are given in Fig. 6. Full details of the various contributions to the total energy ($E_{tot}$) are also included there; see Tan *et al.* (2019) for an explanation of the various parameters. A comparison of the energy frameworks calculated for **II**, showing the electrostatic potential forces ($E_{ele}$), the dispersion forces ($E_{dis}$) and the total energy diagrams ($E_{tot}$), are shown in Fig. 7. The energies were obtained by using the wave function at the HF/3–21 G level of theory. The cylindrical radii are proportional to the relative strength of the corresponding energies [47,23]. They have been adjusted to the same scale factor of 60 with a cut-off value of 6 kJ mol$^{-1}$ within a radius of 6 Å

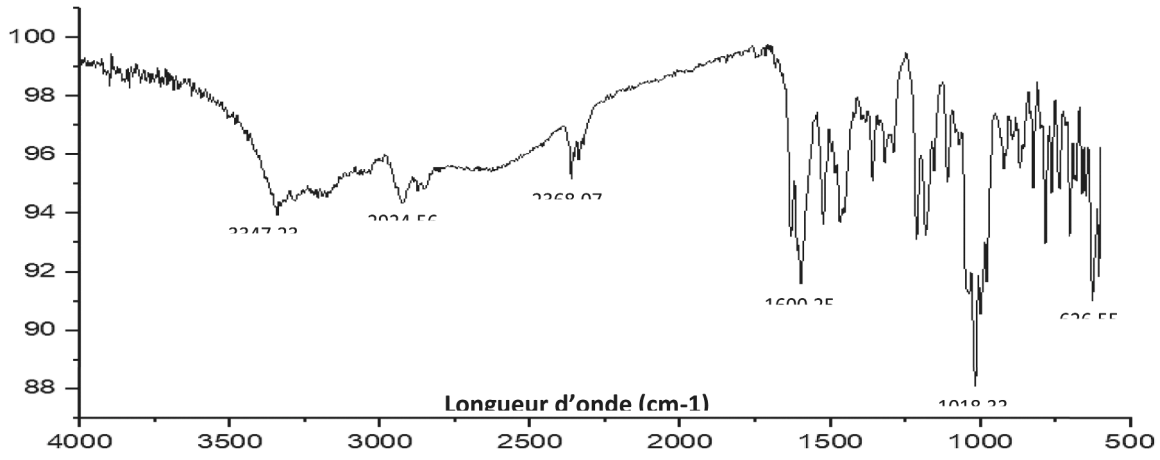


**Fig. 1.** FT-IR Experimental of compound (I).

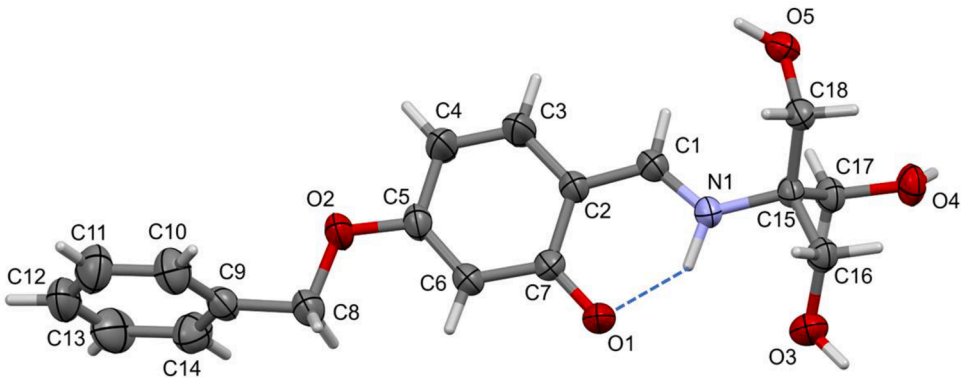


**Fig. 2.** The molecular structure of (II). Displacement ellipsoids are drawn at the 50% probability level. The intramolecular $N^{+}$—H···$O^{-}$ hydrogen bond is shown as a blue dashed line.

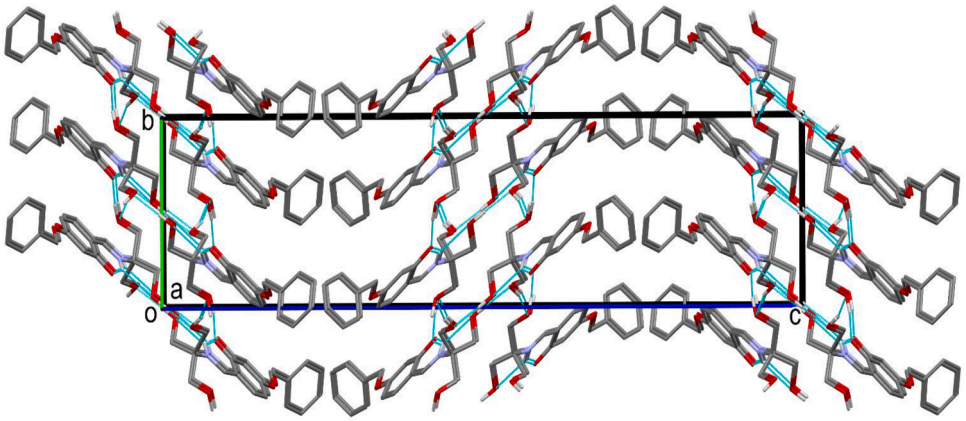


**Fig. 3.** The crystal packing of (II) viewed along the *a*-axis. For clarity, the C-bound H atoms have been omitted. The hydrogen bonds are shown as cyan dashed lines (see Table 2).

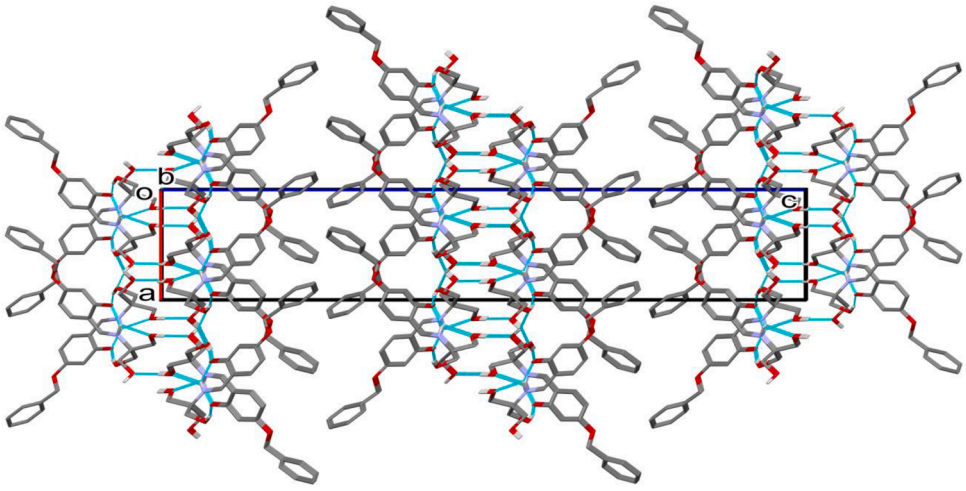


**Fig. 4.** The crystal packing of compound (II) viewed along the *b*-axis. For clarity, the C-bound H atoms have been omitted. The hydrogen bonds are shown as cyan dashed lines (see Table 2).

of a central reference molecule. The major contribution to the intermolecular interactions is from electrostatic potential forces ($E_{ele}$), reflecting the presence of the charge assisted $N^{+}$—H···$O^{-}$ hydrogen bond and the O—H···O hydrogen bonds.

### 3.3. Anti-corrosion results

#### 3.3.1. The open-circuit potentials tests

The determination of equilibrium state by measuring the open circuit potential (OCP) variation with time for the working electrode is necessary before the electrochemical measurement of the corrosion rate. The displacement in OCP values of up to ±85 mV compared to the blank is

**Table 3**
Distances (Å) and angles (°) of hydrogen bond for II.

| D—H···A | d(*D*—H) | d(H···*A*) | d(*D*···*A*) | *D*—H—*A* |
|---|---|---|---|---|
| N1—H1N···O1 | 0.98(2) | 1.791(19) | 2.6217(15) | 140(19) |
| O3—H3O···O4$^{i}$ | 0.91(3) | 1.88(3) | 2.788(2) | 179(3) |
| O4—H4O···05$^{ii}$ | 0.89(2) | 1.91(2) | 2.7675(16) | 162.5(18) |
| O5—H5O···O1$^{iii}$ | 0.94(3) | 1.66(3) | 2.589(2) | 170(2) |
| C1—H1···O5 | 0.9300 | 2.4000 | 3.0593(18) | 128.00 |

Symmetry codes: (i) $-x+2, -y+1, -z$; (ii) $-x+5/2, y+1/2, z$; (iii) $-x+3/2, y-1/2, z$.

an essential parameter that permits the classification of the inhibitor type [48,49]. Fig. 8.A shows the variation of the OCP as a function of time for steel in 0.5 M $H_2SO_4$ in the absence and presence of the inhibitor. In a blank solution, the electrode OCP value was -449 mV vs ECS. The addition of inhibitor converts OCP to more noble values compared to the blank solution. In our case, the difference in the open circuit potential values for inhibitor at 2 mM is -456 vs ECS. From these values, it can be stated that our inhibitors act as mixed-type inhibitors. This result is in good agreement with previous studies [50].

### 3.3.2. *Potentiodynamic polarization studies*

The kinetics and mechanism of the steel anodic dissolution in the sulfuric acid medium have been extensively studied. Potentiodynamic polarization measurements are generally used to obtain relevant information about electrochemical corrosion parameters [51,52]. The Tafel plots of steel API5L grade B in $H_2SO_4$ (0.5 M) for the inhibitor is shown in Fig. 8.B. The electrochemical dissolution of iron can be expressed by the following mechanism [53,54]:

$$Fe \rightarrow Fe^{2+} + 2e^{-}$$

$$2H^{+} + 2e^{-} \rightarrow H_2$$

As shown in Fig. 8.B, the inhibitor's effect on corrosion inhibition reflects on anodic and Cathodic curves to reduce current densities relative to the blank. This displacement is more pronounced in the Cathodic region than this is a Cathodic-type inhibitor. In addition, the value of almost constant tafel slopes decreases for the branches by table without changing the shape of the curves. This means, corrosion kinetics occur without altering the mechanism of the corrosion process controlled by inhibiting activation [48,55].

The polarization curves shift towards positive value with the

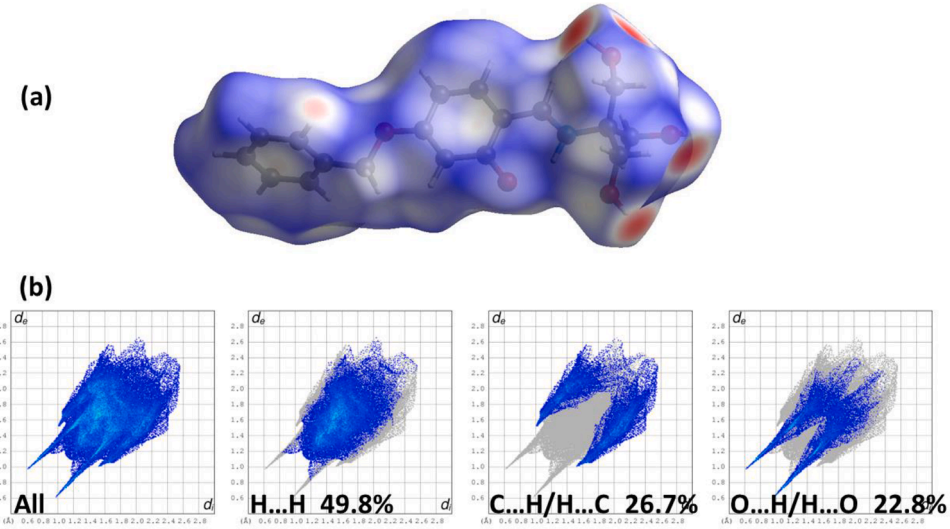


**Fig. 5.** (a) The Hirshfeld surface of II mapped over $d_{norm}$ in the color range −0.7713 to 1.1901 au (b) The full two-dimensional fingerprint plot for II, and those delineated into H···H, C···H/H···C and O···H/H···O contacts. $N^{+}$—H···$O^{-}$.

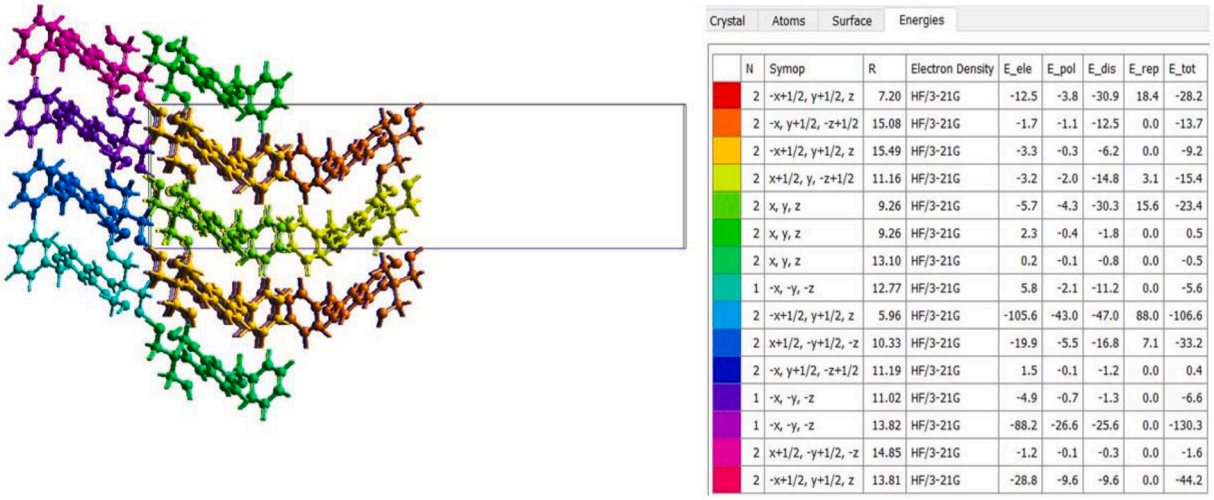


| | N | Symop | R | Electron Density | E_ele | E_pol | E_dis | E_rep | E_tot |
|---|---|---|---|---|---|---|---|---|---|
| | 2 | -x+1/2, y+1/2, z | 7.20 | HF/3-21G | -12.5 | -3.8 | -30.9 | 18.4 | -28.2 |
| | 2 | -x, y+1/2, -z+1/2 | 15.08 | HF/3-21G | -1.7 | -1.1 | -12.5 | 0.0 | -13.7 |
| | 2 | -x+1/2, y+1/2, z | 15.49 | HF/3-21G | -3.3 | -0.3 | -6.2 | 0.0 | -9.2 |
| | 2 | x+1/2, y, -z+1/2 | 11.16 | HF/3-21G | -3.2 | -2.0 | -14.8 | 3.1 | -15.4 |
| | 2 | x, y, z | 9.26 | HF/3-21G | -5.7 | -4.3 | -30.3 | 15.6 | -23.4 |
| | 2 | x, y, z | 9.26 | HF/3-21G | 2.3 | -0.4 | -1.8 | 0.0 | 0.5 |
| | 2 | x, y, z | 13.10 | HF/3-21G | 0.2 | -0.1 | -0.8 | 0.0 | -0.5 |
| | 1 | -x, -y, -z | 12.77 | HF/3-21G | 5.8 | -2.1 | -11.2 | 0.0 | -5.6 |
| | 2 | -x+1/2, y+1/2, z | 5.96 | HF/3-21G | -105.6 | -43.0 | -47.0 | 88.0 | -106.6 |
| | 2 | x+1/2, -y+1/2, -z | 10.33 | HF/3-21G | -19.9 | -5.5 | -16.8 | 7.1 | -33.2 |
| | 2 | -x, y+1/2, -z+1/2 | 11.19 | HF/3-21G | 1.5 | -0.1 | -1.2 | 0.0 | 0.4 |
| | 1 | -x, -y, -z | 11.02 | HF/3-21G | -4.9 | -0.7 | -1.3 | 0.0 | -6.6 |
| | 1 | -x, -y, -z | 13.82 | HF/3-21G | -88.2 | -26.6 | -25.6 | 0.0 | -130.3 |
| | 2 | x+1/2, -y+1/2, -z | 14.85 | HF/3-21G | -1.2 | -0.1 | -0.3 | 0.0 | -1.6 |
| | 2 | -x+1/2, y+1/2, z | 13.81 | HF/3-21G | -28.8 | -9.6 | -9.6 | 0.0 | -44.2 |

**Fig. 6.** The color-coded interaction mapping within a radius of 6 Å of a central reference molecule of II.

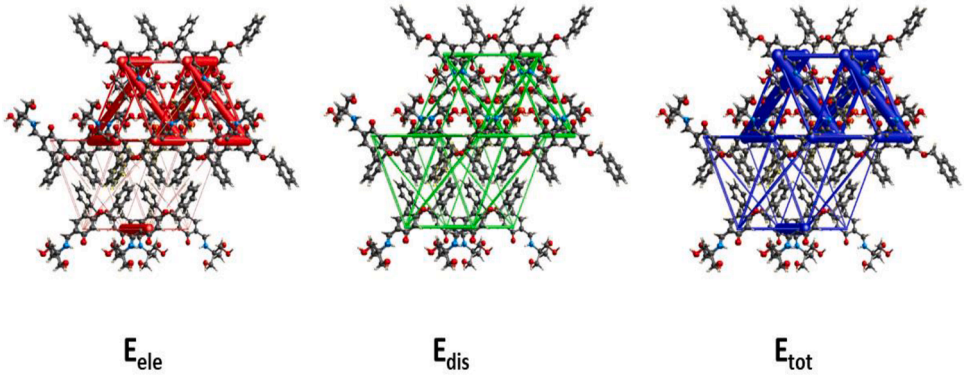


**Fig. 7.** The energy frameworks calculated for II viewed along the *a*-axis direction, showing the electrostatic potential forces ($E_{ele}$), the dispersion forces ($E_{dis}$) and the total energy diagram ($E_{tot}$).

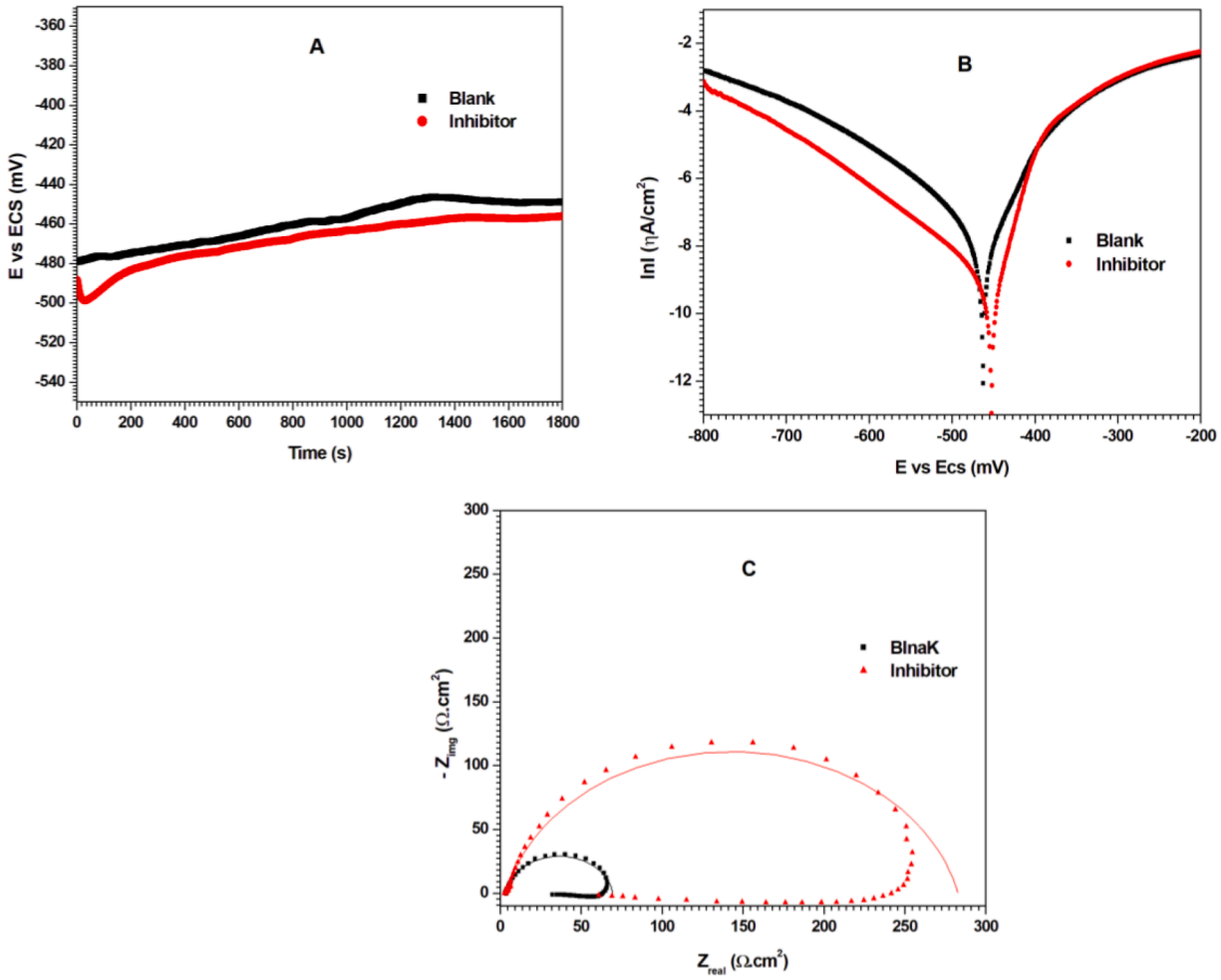


**Fig. 8.** Open circuit potential (A), Potentiodynamic polarization curves (B) and Nyquist plot (C) of steel API5L grade B immersed in 0.5 M $H_2SO_4$ with and without inhibitor.

increasing of inhibitors presence. Since the offset of the $E_{corr}$ value is less than 85 mV, we can classify the studied organic compound as mixed-type inhibitor [48,50,56].

The electrochemical corrosion parameters corrosion currents densities ($I_{corr}$), corrosion potentials ($E_{corr}$), anodic and cathodic Tafel slopes ($\beta_a$ and $\beta_c$) have been obtained by Tafel extrapolation method of the polarization curves and obtained values are listed in Table 4. The Table 4 shows that the efficiency inhibition 78.53%.

### 3.3.3. *Impedance measurements*

To study the surface properties of steel and the mechanism of processes effect on the electrode, we performed electrochemical impedance measurements on API5L grade B steel in 0.5 M $H_2SO_4$ solution with and without the inhibitor. The results are shown in Fig 8.C.

To obtain information about the double layer, we performed electrochemical impedance spectroscopy measurements. As shown in Fig 8. C, all high-frequency loops have the format of compressed half circles. This is the result of the scattering factors due to the inhomogeneity of the

**Table 4**
Polarization measurements for steel API5L grade B corrosion in the absence and presence of inhibitor at 2 mM concentration.

| | $E_{corr}$(mV/ ECS) | $\beta_a$(mV/ dec) | $\beta_c$(mV/ dec) | $I_{corr}$(μA. $cm^{-2}$) | *EI (%)* |
|---|---|---|---|---|---|
| Blank | 463 | 118.7 | 118.7 | 341 | |
| Inhibitor | −452 | 85.4 | 179.3 | 73.2 | 78.53 |

working electrode [57]. The diameters of these capacitive loops increase with in the presence of inhibitor which means the increase of resistance (Rct), that is, of the charge transfer process. In addition, inductive loops are found in the low frequency region which infers adsorption and non-desorption of corrosion intermediates and corrosion inhibitors [58, 59]. The amplitude of the inductive loops increases with the inhibitor with no difference in the shape of the curves, which means that the different steps that determine the corrosion mechanism do not change [60].

The impedance data obtained above was analyzed using an electrochemical equivalent circuit shown in Fig. 9 and Table 5, where $R_s$, $R_{ct}$ and CPE are the resistance solution, charge transfer resistance and constant phase element, respectively. The term CPE was introduced to replace a double-layer capacitance ($C_{dl}$) for a more accurate fit. The impedance constant phase element ($Z_{CPE}$) is represented by [61]:

$$Z_{CPE} = \frac{1}{Y_0(J\omega)^n} \tag{11}$$

$Y_0$ is a proportionality coefficient, j: imaginary unit ($j^2 = -1$), n is a CPE exponent with values between 0 and 1 and can be used to gage the surface inhomogeneity, ω is the angular frequency given by $\omega = 2\pi f_{max}$. The CPE components $Y_0$ and n were used in the calculation of the double-layer capacitance ($C_{dl}$) of the adsorbed film following Eq. (4) [61]:

$$Cdl == (\mathrm{Y0.Rct1} - n)1/n \tag{12}$$

As shown by the solid lines in Fig. 8.C, the accuracy of the equivalent circuit fit was verified by plotting the simulated Nyquist curves. These data indicate that with increasing inhibitor, the EPC values decrease and $R_{ct}$ increases. The decrease in capacitance that results from a reduction in the dielectric constant and/or an increase in the thickness of the electrical double layer suggest that the inhibitor studied acts by adsorption on the metal/electrolyte interface [62,63]. In this case, it can be assumed that the inhibitor replaces the adsorbed water molecules on the steel surface. The inhibition efficiency was increased to more than 76% at 2 mM, confirming the obtained results in the polarization curve method.

### 3.4. DFT calculations

#### 3.4.1. DFT-optimized geometry

The ωB97XD/6–311+*g*(d) fully optimized structures of **III** is illustrated in Fig. 10, where selected geometrical parameters in the gas phase and in solvent are given in Table 6. The equilibrium bond distances, angles and value of Root Mean Square Errors (RMSE) are listed in the Table 6.

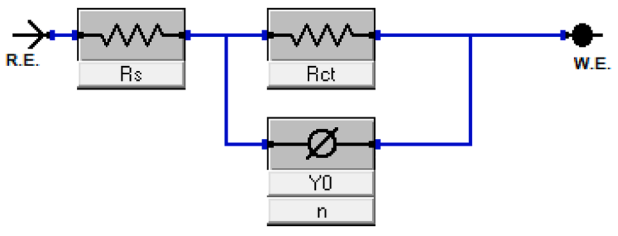


**Fig. 9.** Equivalent circuit diagrams used to fit impedance data.

**Table 5**
Impedance parameters for steel API5L grade B in 0.5 M $H_2SO_4$ solution in the absence and presence of inhibitor.

| $C_{inh}$ (mM) | $R_s$ (Ω. $cm^2$) | $R_{ct}$ (Ω. $cm^2$) | *n* | $Y_{0\ 0}.10^{-6}$ ($S^n.cm^2.\ \Omega^{-1}$) | $C_{dl}$ (μF. $cm^{-2}$) | *IE* (%) |
|---|---|---|---|---|---|---|
| Blank | 3.424 | 66.07 | 0.9186 | 130.7 | 84.1 | |
| Inhibitor | 3.271 | 279.6 | 0.8553 | 82.30 | 55.3 | 76.36 |

The optimized structures of the title compound compare well with the experimental data. In particular, the C15-N1, C1-C2 and C5-O2 calculated bond lengths in gas and solvent are smaller than the experimental values (~ 0.017, 0.012 and 0.017 Å, respectively) whereas the N1-C1 is longer than the experimental about 0.025 Å. Furthermore, the superposition of the X-ray crystallography structure and the optimized geometry of **III** is illustrated in Fig. 11, and the value of root-mean-square errors is 0.306, 0.343, 0.343, 0.344 and 0.356 Å in chloroform, methanol, acetonitrile, water and gas, respectively. These results indicate that the no-polar solvent (chloroform) displays a lower value of RMS error than the polar solvent. From this result, we can conclude that the calculated geometries (bond lengths and bond angles) are in excellent agreement with the experimental data.

On the other hand, the analysis of the calculated thermodynamic parameters at 298.15 K in Table 6 demonstrated a weak significant effect of the solvents on the enthalpy (H°), Gibbs energy (G°) and molar heat capacity (Cv) of the title compound, with an increase in the entropy values in the solvent (about 3.34 Cal/Mol.K).

#### 3.4.2. Inhibition mechanism

In order to study the reaction between the inhibitor molecule and bulk metal surface (Fe and Cu) the global and local reactivity indexes were calculated and listed in Tables 7 and 8. From our quantum chemical calculations, we can see that the gas phase showed the largest values of the chemical hardness indicating greater stability of **III**, whereas the lowest value of hardness was observed in the solvent. The overall increasing order of hardness in the studied compound was as follows: η(water)> η(acetone)> η(methanol)> η(chloroform). On the other hand, the potential chemistry of **III** is larger in gas than that in the solvent. These results indicate that the tendency of the electrons to leave the equilibrium inhibitor compound increases from gas and non-polar to polar media. In other words, the increase of the μ values indicates that **III** demonstrate a highest tendency to donate electrons in Chloroform than in any other solvent. According to the global electrophilicity scale [64, 65] the inhibitor molecule **III** can be classified as moderate electrophiles (0.891 to 0.962 eV).

The electronegativity (χ) assigns the flow of electron directions' between the metal surface and the inhibitor compound till a balance in chemical potential is attained. On adsorption of inhibitor molecule on the metal surface, particularly iron and copper with electronegativity 7 and 4.9 eV, respectively [66–68], electrons should be transferred in the system from the less to the most electronegative. According to our calculation, **III** displays less electronegativity than iron and copper suggesting that they is eligible of electron transfer to the metal surface and the inhibitor will present good kinetic interaction with the iron than the copper surface.

The number of transferred electron ($\Delta N_{M/Metal}$) is a successful quantum chemical descriptor that helps studying the interactions metal-inhibitor. Our calculation in Table 7 indicated that the $\Delta N_{Mi/Metal}$ value of **III**/Fe was three folds larger than the **III**/Cu, indicating an excellent interaction between the corrosion inhibitor and the iron surface in both gas and solvent. Parallelly, in gas and non-polar media (chloroform), compound **III** displays a largest $\Delta N_{Mi/Metal}$ value indicating that it has a greater potential of releasing electron into low-lying vacant d-orbitals of the metal [66] than the methanol, acetone and water, respectively. The corrosion inhibitor with weak electrophilicity (ω) displays a good

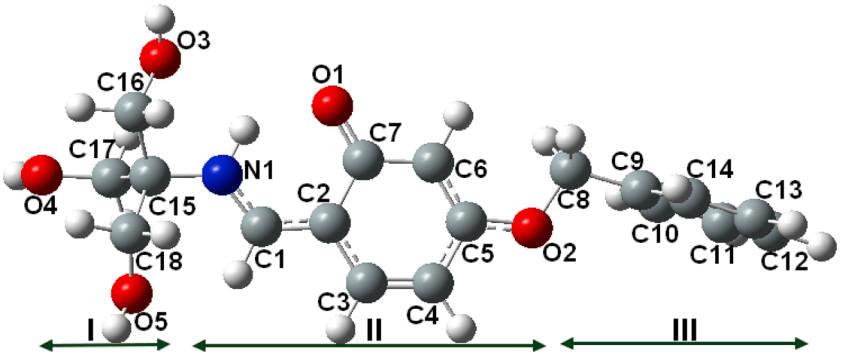


**Fig. 10.** Optimized geometry of I, *i.e.* structure III (see Scheme).

**Table 6**
Thermodynamic and structural parameters calculated in gas and different solvents at room temperature, using ωB97X-D/6–311+*g*(d) level theory.

| | Exp. | Gas (ε=1) | chloroform (ε=4.711) | methanol (ε=32.613) | acetonitrile (ε=35.688) | water (ε=78.355) |
|---|---|---|---|---|---|---|
| H | – | −1128.90 | −1128.92 | −1128.93 | −1128.93 | −1128.93 |
| G | – | −1128.98 | −1128.99 | −1129.01 | −1129.01 | −1129.01 |
| Cv (Cal/Mol-K) | – | 86.115 | 87.428 | 87.399 | 87.400 | 87.410 |
| S (Cal/Mol-K) | – | 164.584 | 168.823 | 167.671 | 167.663 | 167.716 |
| C15-N1 (Å) | 1.479 | 1.454 | 1.463 | 1.465 | 1.465 | 1.465 |
| N1-C1 (Å) | 1.291 | 1.322 | 1.318 | 1.315 | 1.315 | 1.314 |
| C1-C2 (Å) | 1.409 | 1.392 | 1.396 | 1.400 | 1.400 | 1.400 |
| C5-O2 (Å) | 1.367 | 1.349 | 1.350 | 1.349 | 1.349 | 1.349 |
| O2-C8 (Å) | 1.427 | 1.419 | 1.428 | 1.430 | 1.430 | 1.431 |
| O2-C8-C9 (°) | 107 | 109 | 108 | 108 | 108 | 108 |
| C15-N1-C1 (°) | 127 | 128 | 126 | 127 | 127 | 128 |
| C15-N1-C1-C2 (°) | −177 | −179 | 178 | −177 | −177 | −177 |
| RMS Error (Å) | – | 0.362 | 0.306 | 0.343 | 0.343 | 0.344 |

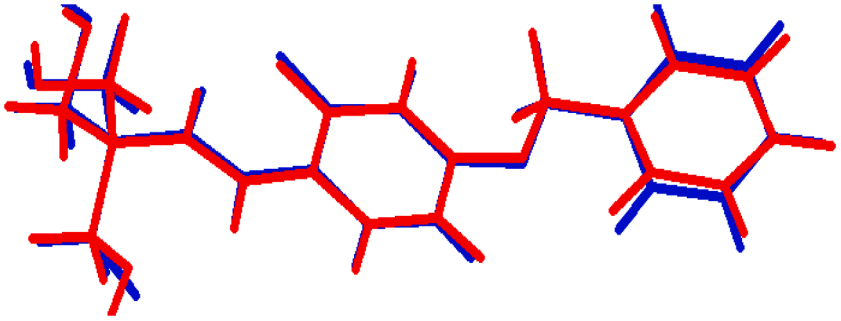

**Fig. 11.** Atom-by-atom superimposition of the X-ray structure (blue) over the calculated geometry (red) of title compound (III).

**Table 7**
Chemical potential (μ), Chemical hardness (η), global electrophilicity index (ω) and fraction of the transferred electron (ΔN).

| | μ (eV) | η (eV) | ω (eV) | $\Delta N_{III/Fe}$ | $\Delta N_{III/Cu}$ |
|---|---|---|---|---|---|
| Gas | −3.674 | 7.570 | 0.891 | 0.219 | 0.086 |
| Chloroform | −3.690 | 7.627 | 0.893 | 0.216 | 0.084 |
| Methanol | −3.827 | 7.664 | 0.955 | 0.206 | 0.075 |
| Acetone | −3.829 | 7.665 | 0.956 | 0.205 | 0.075 |
| Water | −3.843 | 7.669 | 0.962 | 0.205 | 0.074 |

electron releasing potential for efficient interaction with stabilization on a metal surface (Fe and Cu, respectively). This property increases in the order ω(water)> ω(acetone)> ω(methanol)> ω(chloroform). Succinctly, gas and non-polar media displayed close chemical reactivity values, indicating considerable contribution of these media to corrosion inhibition potential while polar solvent does not appear to exert any improvement of the chemical reactivity. The comparison of the local reactivity indices results presented in Table 3 suggests the following explanation. The sites with the highest values of condensed Fukui functions $f^-$ and $f^+$ are those for the electrophilic and nucleophilic attack, respectively. Furthermore, the most reactive site for electrophilic attack by corrosion inhibitor is on the C7 atom. The dual descriptor

$\Delta f(r)$ and local philicity index in gas and solvent show that the favorable site for a nucleophilic attack is C7 (have a largest $\Delta f(r)$ and ($\Delta\omega^+$).

These results lead to the conclusion that **III** can bond more strongly to the surface of iron atoms rather than copper atoms surface, thus providing effective protection against corrosion in chloroform rather than in polar environments. The dominant interaction was between the metal atom and atom C7 of the corrosion inhibitor (**III**) as shown in Fig. 12.

### *3.4.3. Observed and calculated UV–vis absorption spectra with different solvents*

The electronic spectral analysis of the title compound was calculated in both gas and various polar and nonpolar solvent phases by using the time dependent-DFT method (TD-DFT) and polarizable continuum

**Table 8**
Local reactivity descriptors were calculated for the corrosion inhibitor in gas and solvent.

| | Gas (ε=1) | | chloroform (ε=4.711) | | methanol (ε=32.613) | | acetonitrile (ε=35.688) | | Water (ε=78.355) | |
|---|---|---|---|---|---|---|---|---|---|---|
| Atom | Δf(r) | Δω | Δf(r) | Δω | Δf(r) | Δω | Δf(r) | Δω | Δf(r) | Δω |
| O1 | −0.0939 | −0.003 | −0.1171 | −0.006 | −0.1261 | −0.008 | −0.1261 | −0.008 | −0.1268 | −0.009 |
| O2 | −0.0013 | 0.000 | 0.0052 | 0.000 | 0.0068 | 0.000 | 0.0068 | 0.000 | 0.0070 | 0.000 |
| O3 | −0.0017 | −0.000 | −0.0016 | 0.000 | −0.0016 | 0.000 | −0.0016 | 0.000 | −0.0016 | 0.000 |
| O4 | 0.0019 | 0.000 | 0.0018 | 0.000 | 0.0023 | 0.000 | 0.0023 | 0.000 | 0.0024 | 0.000 |
| O5 | −0.0013 | 0.000 | 0.0038 | −0.000 | 0.0028 | −0.000 | 0.0028 | −0.000 | 0.0024 | −0.000 |
| N6 | −0.0309 | −0.001 | −0.0171 | −0.000 | −0.0045 | −0.000 | −0.0068 | −0.000 | −0.0058 | −0.000 |
| **C7** | **0.2307** | **0.008** | **0.253** | **0.013** | **0.246** | **0.017** | **0.2604** | **0.018** | **0.261** | **0.018** |
| `C8 | −0.0811 | −0.007 | −0.0830 | −0.012 | −0.1082 | −0.014 | −0.0913 | −0.016 | −0.0921 | −0.016 |
| C9 | 0.0669 | 0.003 | 0.0975 | 0.006 | 0.0980 | 0.007 | 0.1041 | 0.008 | 0.1048 | 0.008 |
| C10 | −0.1753 | −0.006 | −0.1903 | −0.010 | −0.1996 | −0.013 | −0.2001 | −0.013 | −0.2011 | −0.014 |
| C11 | 0.0749 | 0.004 | 0.0733 | 0.007 | 0.0742 | 0.009 | 0.0743 | 0.009 | 0.0744 | 0.009 |
| C12 | −0.0767 | −0.002 | −0.0840 | −0.004 | −0.0909 | −0.006 | −0.0899 | −0.006 | −0.0904 | −0.006 |
| C13 | 0.0451 | 0.003 | 0.0591 | 0.005 | 0.0717 | 0.006 | 0.0712 | 0.006 | 0.0726 | 0.006 |
| C14 | −0.0016 | 0.000 | 0.0001 | 0.000 | 0.0005 | 0.000 | 0.0005 | 0.000 | 0.0005 | 0.000 |
| C15 | 0.0005 | 0.000 | 0.0013 | 0.000 | 0.0015 | 0.000 | 0.0015 | 0.000 | 0.0015 | 0.000 |

model at the TD-ωB97XD/6-311g(d) level theory on the ground state optimized geometry. The results of the computed absorption spectrum, wavelength (nm), electronic transition of excitation energy (eV) and oscillator strengths ($f_{os}$), the excitation from the electronic ground states of occupied orbitals to the virtual ones, unoccupied orbital and the absorption properties of title compound are demonstrated in Table 9 and Fig. 13.

As results from Fig. 13 the corrosion inhibitor (**III**) showed high-intensity band at ~ 278 nm in all three solvents, which can be attributed to the n, π →π* electronic transition (see Table 9). From TD-DFT calculation, a strong absorption band was observed at 260 nm ($f$ = 0.502) and 257 nm ($f$ = 0.557) in the gas and solvent phases, respectively, which corresponds to the electronic transition from HOMO-1 to LUMO (70%). On the other hand, the absorption wavelengths of transition HOMO→LUMO in gas and solvent phases are located at 329 nm ($f$ = 0.269) and 328 nm ($f$= ~0.346), respectively (Fig. 13b and Fig. 14). We can note that with the increasing solvent polarity from non-polar to polar, the oscillator strengths values display a slight increase for the electronic transition HOMO→LUMO and HOMO-1→LUMO. This difference can be attributed to the solvent effects on the electrostatic structure [69] and the molecular orbital of M. The HOMO orbital showed that π-bonding and non-bonding (n-type) molecular orbitals were identified on the II moiety and on the O1, and N6 atoms, the HOMO-1 orbital was localized on the II moiety and oxygen and nitrogen atoms (O1, O2 and N6). Similarly, the LUMO showed the π* anti-bonding type orbitals on carbon, oxygen and nitrogen atoms were localized in the II fragment (see Figs. 10 and 14). Furthermore, the simulated spectra of **III** was red-shifted in comparison to the experimentally obtained data ($\lambda_{exp}$= +~18 nm). Moreover, an excellent agreement was observed between the TD-DFT and experimental absorption spectra results.

**Table 9**
The calculated and experimental excited state transition wavelength ($\lambda_{Cal.}$ and $\lambda_{exp.}$ nm), oscillator strengths ($f$) and molecular orbital transition of the studied compound.

| E (eV) | $\lambda_{Cal.}$ | $\lambda_{exp.}$ | $f$ | Electronics transitions | |
|---|---|---|---|---|---|
| Gas | | | | | |
| 3.773 | 329 | – | 0.269 | H→L | π, n→π* (n in O1 and N6 atoms) |
| 4.774 | 260 | – | 0.502 | H-1→L | π, n→π* (n in O1, O2 and N6 atoms) |
| 5.630 | 220 | – | 0.231 | H→$L$ + 9 | π, n→π* |
| Chloroform (ε=4.711) | | | | | |
| 3.742 | 331 | 375 | 0.356 | H→L | π, n→π* (n in O1 and N6 atoms) |
| | | 300 | | | |
| 4.793 | 259 | 277 | 0.577 | H-1→L | π, n→π* (n in O1, O2 and N6 atoms) |
| 5.550 | 223 | | 0.351 | H→$L$ + 8 | π, n→π* |
| Acetonitrile (ε=35.688) | | | | | |
| 3.781 | 328 | 310 | 0.344 | H→L | π, n→π* (n in O1 and N6 atoms) |
| 4.813 | 258 | 279 | 0.555 | H-1→L | π, n→π* (n in O1, O2 and N6 atoms) |
| 5.568 | 223 | | 0.379 | H→$L$ + 5 | π, n→π* |
| methanol (ε=32.613) | | | | | |
| 3.782 | 328 | – | 0.342 | H→L | π, n→π* (n in O1 and N6 atoms) |
| 4.815 | 257 | – | 0.552 | H-1→L | π, n→π* (n in O1, O2 and N6 atoms) |
| 5.570 | 223 | – | 0.376 | H→$L$ + 5 | π, n→π* |
| Water (ε=78.355) | | | | | |
| 3.784 | 328 | 320 | 0.343 | H→L | π, n→π* (n in O1 and N6 atoms) |
| 4.816 | 257 | 278 | 0.552 | H-1→L | π, n→π* (n in O1, O2 and N6 atoms) |
| 5.570 | 223 | | 0.381 | H→$L$ + 5 | π, n→π* |

### 3.5. Molecular docking

The best binding pose of **SB** compound at the active site of 2Y9X is represented in Fig. 15, and the associated calculated parameters are given in Table 10.

Based on the docking results (Table 11), SB compound exhibited significant ability to inhibit the target protein 2Y9X, with a free energy of binding of −6.16 kcal/mol and estimated inhibition constant of KiC 30.45 uM.

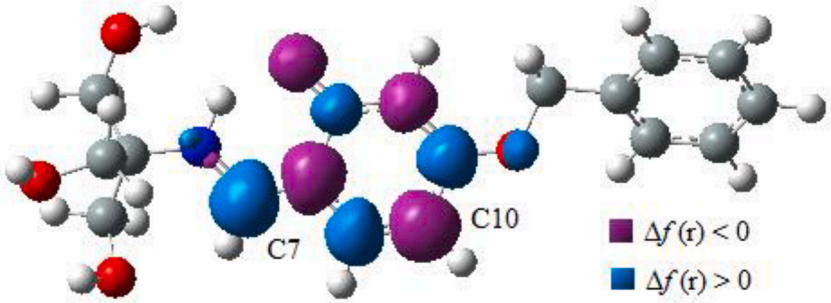


**Fig. 12.** Maps of the dual descriptor of (III).

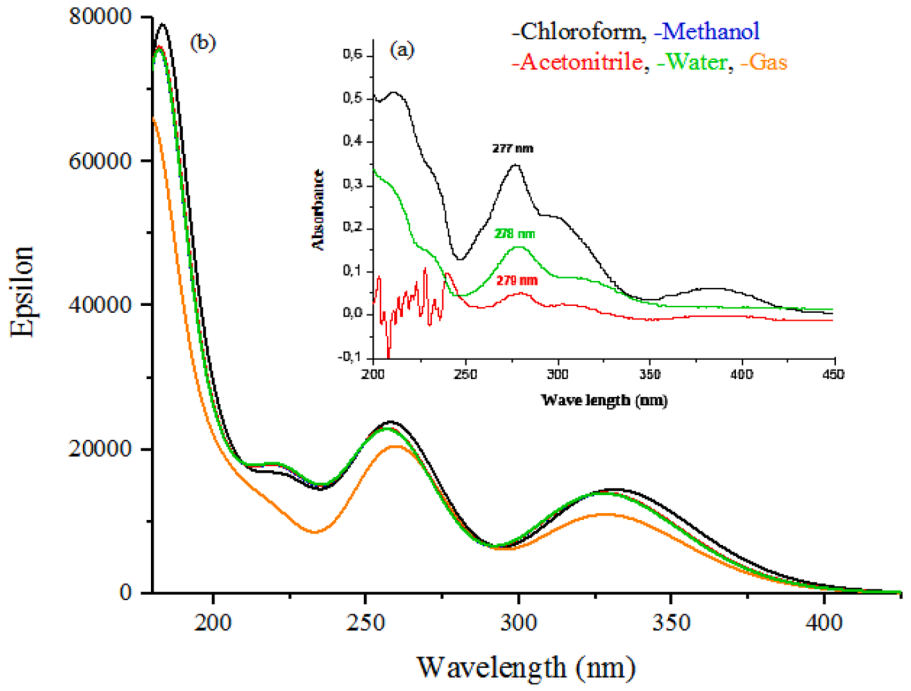


**Fig. 13.** (a) Experimental absorption spectrum of the titled compound in gas and different solvents at room temperature; (b) TD-DFT calculated absorption spectrum in the gas phase and different solvents.

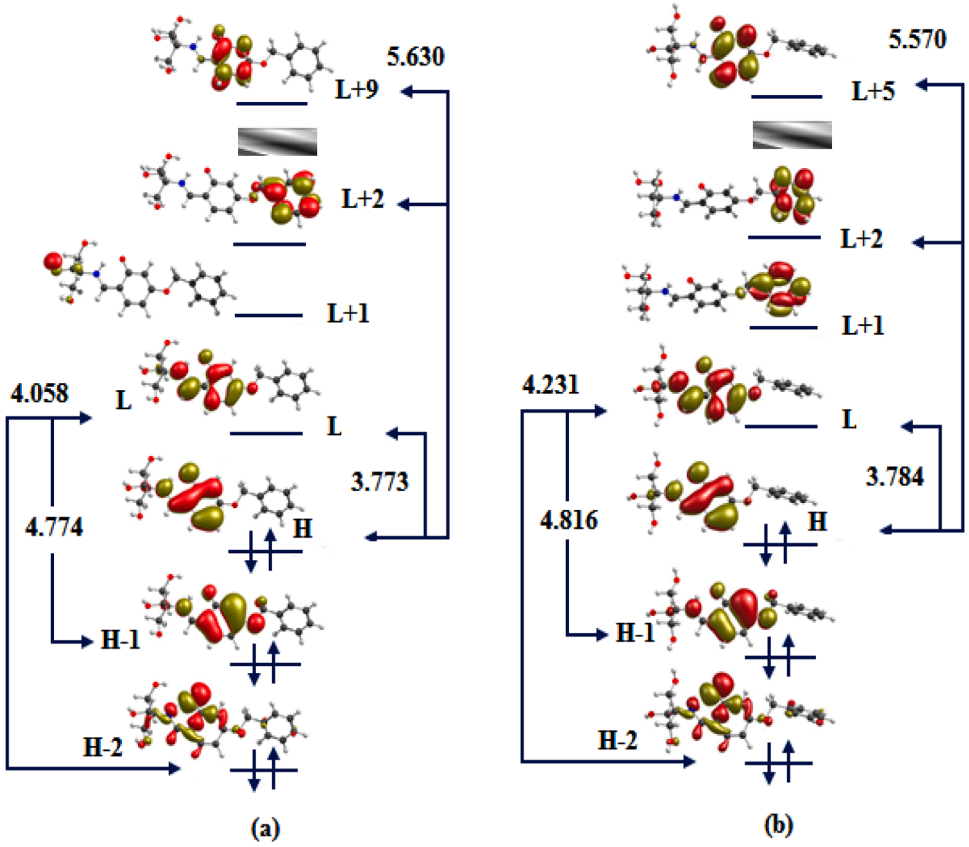


**Fig. 14.** Frontier molecular orbitals contributing to the electronic absorption along with band gap (ΔE) in the gas (a) and water (b) for compound (III).

Our results regarding this binding affinity between SB and 2Y9X are relatively higher than those obtained by Roselan.M.A. and co-workers [70] who have studied the interaction of Kojic monooleate (KMO) and kojic acid (KA) compounds with mushroom tyrosinase (2Y9X) by means of molecular docking, and found that the KMO and KA shows strong binding interactions against 2Y9X target enzyme, with binding energies

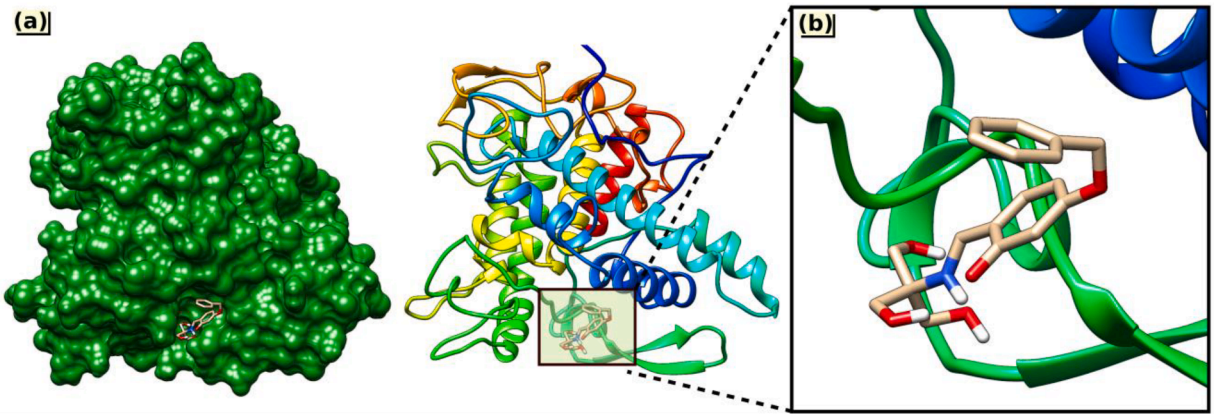


**Fig. 15.** The best binding pose of SB compound at the active site of 2Y9X protein; a) molecular surface view, b) 3D ligand interaction diagram.

**Table 10**
Calculated parameters [a-f] of the best binding pose of SB compound at the active site of 2Y9X protein.

| Parameters | Protein-ligand complex 2Y9X@SB |
|---|---|
| **BE** | −6.16 |
| **KiC** | 30.45 |
| **RMSD** | 0.96 |
| **TIE** | −9.44 |
| **EE** | −0.35 |
| **FIE** | −2.99 |

[a] BE: Free Energy of Binding (kcal/mol).
[b] RMSD: Root-Mean-Square Deviation.
[c] KiC: Estimated Inhibition Constant, Ki. (uM: micromolar).
[d] TIE: Total intermolecular energy (kcal/mol).
[e] EE: Electrostatic Energy (kcal/mol).
[f] FIE: Final Total Internal Energy (kcal/mol).

**Table 11**
Amino acid residues involved in the interactions of SB compound at the active site of 2Y9X protein.

| Complex | *Amino acid involved in interaction (Interaction site)* | Distances (Å) |
|---|---|---|
| **2Y9X@SB** | **Gln41(A), Lys158(A), Glu173(A), His178 (A), Asn174(A), Gln44(A)** & **Ala45(A).** | **SB—Gln41(A)** (2.83,3.39) **SB—Glu173(A)** (2.29,2.55, 2.12) **SB—Lys158(A)** (2.02) **SB—His178(A)** (2.05) **SB—Asn174(A)** (1.88, 2.96) **Lig—Gln44(A)** (4.29) **Lig— Ala45(A)** (4.61) |

of −5.70 and −4.01 kcal/mol.

The 2D and 3D visualizations of 2Y9X@SB complex for the best binding mode with amino acid residues involved in the interactions are presented in Fig. 16, and in Table 11, we provided a list of amino acids involved in the interactions associated with their distances (Å) between them and the SB ligand.

Accordnigly, the molecular docking results (Fig. 16 and Table 11) revealed that the SB formed six conventional hydrogen bonds with the active site of 2Y9X including amino acid residues of Asn174(A), His178 (A), Gln41(A), Lys158(A), Phe215(B) and two interactions with Glu173 (A). All the hydrogen bond distances between the corresponding amino acids and SB compound are found in a range of 1.88–3.39 Å.

In addition, SB compound interacted with the binding site of the 2Y9X receptor through one salt bridge including Glu173(A) residue, one π-alkyl interactions with Ala45(A) and one Amide-π stacked interaction with amino acid residue of Gln44(A), as depicted in Fig. 16 and Table 11.

### 3.6. Antioxidant activity

Due to their interdisciplinary importance in different domains, Schiff-base ligands have played a significant role in the evolution of contemporary coordination chemistry and its future prospects as potential bioactive drug starters. These molecules have been largely studied in several fields of chemistry in particular, regarding their eventual applications, mainly in biological: antimicrobial, redox, catalytic, and antioxidant activities [71] but also for their medical applications as antibacterial [72,73] and antifungal [74] (including anti-yeast), antiviral [75,76], antitumor [77,78], anti-inflammatory [79], antipyretic, antimalarial, anticancer [80–82], anesthetic, oxytocin imitating and oxytocin-inhibiting compounds, and also as selective inhibitors targeting human tyrosine phosphatase 1B (PTP1B) or TCPTP and SHP-1 tyrosine phosphatases [83–85].

Five different methods were performed to investigate the in vitro antioxidant activity of our compounds. Our compound showed a mild scavenging capacity for ABTS radicals with $IC_{50}$ values of 196.52±1.06 μg/mL, however, the tested compound did not show any significant effect in the rest of the antioxidant testing methods (>200 μg/mL). These values and despite being mild, remain significantly higher than the recorded values by the tested standards (BHA, BHT, Trolox and Vitamin C).

The chelating activity of Schiff base ligands is mainly associated with the presence of nitrogen in the imine groups (C = N) in Schiff-bases and in their metallic complexes, thus, their chelating properties are the reason for their many unique biological properties [71].

Nevertheless of the higher efficiency of these ligands compared to their respective complexes, there are indeed mentions of free ligands being more effective than their respective complexes [86], most often, it is the complexes of Schiff bases and metal ions that exhibit the strongest of the above-mentioned biological properties [86,87], which may explain the mild capacity of our compound leading us to suggest that the respective metallic complex of this later may serve as a better model for a synthetic antioxidant compound in experimental biological systems.

## 4. Conclusions

In this paper,the zwitterion (*E*)−2-((4-(benzyloxy)−2-hydroxybenzylidene)amino)−2-(hydroxymethyl)propane-1,3-diol (**I**), was synthesized and the structure characterized by X-ray diffraction analysis and by IR, $^{1H}$NMR , $^{13C}$-NMR spectroscopies. The major interatomic and intermolecular interactions have been discussed and explained; its

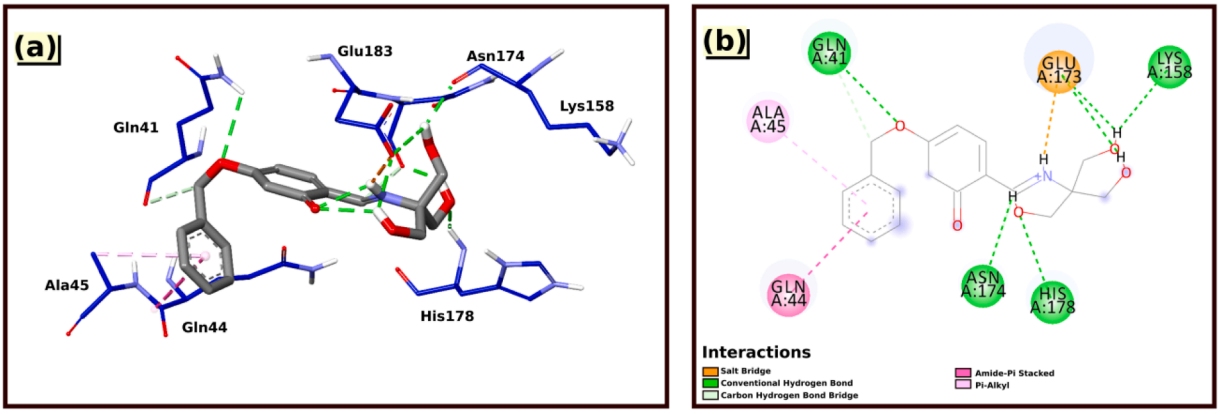


**Fig. 16.** Representations of 2Y9X@SB complex for the best binding mode with amino acid residues involved in the interactions; (a) 3D visualization, (b) 2D visualization.

potential antioxidant properties were assessed in vitro and *in silico* and revealed to be mild speculating its potential therapeutic properties in future drug design; whereas its high chemical hardness and chemical potential as an anti-corrosive agent emphasizes its possible use in the metals industry,and this compound is a promising anti-oxidant and anti-corrosive agent. Therefore, enlarged experiments applied to more complex chemical and biological systems are required in order to establish the mechanisms of action and other eventual targets and properties related to its molecular structure. Corrosion inhibition potentials of the title compound have been investigated using quantum chemical calculations at ωB97XD with 6–311+*g*(d) basis set in gas and solvents. Our results show that the title compound exhibit high chemical hardness and chemical potential in gas than that in the solvent. The number of transferred electrons from **III** to the low-lying vacant d-orbitals of iron indicates good corrosion mitigation potentials. The Fukui indices, local philicity index and dual descriptor suggest that the C7 atom is the nucleophilic sites on the inhibitor for effective interaction on the metal surface. On the other hand, TD-DFT calculations show an excellent correlation with the UV–vis absorption assigned to π→π* and n→π* transitions.

## Credit author statement

Redouene Lemoui, Elaboration, Writing and proposed; Douniazed Hannachi, Theoretical calculations, Interpretation, Methodology and Writing. Helen Stoeckli-Evans, Writing, crystallography discussion and structural resolution; Amel Djedouani, Methodology and Writing crystallography part; Mohamed Zabat, Antioxidant activity experimentally; Hocine Merazig, Registration and structural resolution. Hamza Allal, Docking part; Iman Ramli, Language reviewer; Said Mohamed el hadi, Analytical part; Imane Habila, Antioxidant activity discussion and Writing; Nadir Ghichi, Supervisor, Elaboration, Writing and reviewer of parts

## Declaration of Competing Interest

The authors declare that they have no known competing financial interests or personal relationships that could have appeared to influence the work reported in this paper.

## Data availability

No data was used for the research described in the article.

## Acknowledgments

The authors thanks the unit of research CHEMS, Chemistry Department, University of Mentouri Brothers, Constantine 1, Algérie, for financing the study, for their collaboration in this research, Also, the authors are very grateful to the “ University of Lyon, University of Claude Bernard Lyon 1, CNRS UMR 5280, Institute of Analytical Sciences, 69622 Villeur banne Cedex, France, for offering the computing facilities, and Institute of Physics, University of Neuchâtel, 2000 Neuchâtel, Switzerland for their collaboration with our team.

## Supplementary materials

Supplementary material associated with this article can be found, in the online version, at doi:10.1016/j.molstruc.2023.135569.

## References

[1] S.M. Lee, K.S. Sim, K.M. Lo, Synthesis, characterization and biological studies of diorganotin (IV) complexes with tris [(hydroxymethyl) aminomethane] Schiff base, Inorg. Chim. Acta. 429 (2015) 195–208, https://doi.org/10.1016/j.ica.2015.01.017.
[2] A. Xavier, N. Srividhya, Synthesis and study of Schiff base ligands, IOSR J. App. Chem. 7 (11) (2014) 06–15, https://doi.org/10.9790/5736-071110615.
[3] & T.P. Yoon, E.N. Jacobsen, Privileged chiral catalysts, Science 299 (5613) (2003) 1691–1693.
[4] A. M. Abu-Dief, and I M A. Mohamed. "A review on application of transition metal complexes incorporating Schiff bases." (2015), doi: 10.1016/j.bjbas.2015.05.004.
[5] M. Yoshizawa, M.Kawano T.Kusukawa, T. Ohhara, I. Tanaka, K. Kurihara, N. Niimura, M. Fujita, Endohedral clusterization of ten water molecules into a “molecular ice” within the hydrophobic pocket of a self-assembled cage, J. A. Chem. Soc. 127 (9) (2005) 2798–2799, https://doi.org/10.1021/ja043953w.
[6] Y.K. Tyagi, A. Kuma, H.G. Ray, P. Vohra, G. Gupta, R. Kumari, P. Kumar, R. K. Kupta, Synthesis of novel amino and acetyl amino-4-methylcoumarins and evaluation of their antioxidant activity, Eur. J. Med. Chem. 40 (4) (2005) 413–420, https://doi.org/10.1016/j.ejmech.2004.09.002.
[7] A. Jezierska-Mazzarello, R. Vuilleumier, J.J. Panek, C. Ciccotti, Molecular property investigations of an ortho-hydroxy Schiff base type compound with the first-principle molecular dynamics approach: the, J. Phy. Chem. B 114 (1) (2010) 242–253, https://doi.org/10.1021/jp903501m.
[8] S.D. Chatziefthimiou, Y.G. Lazarou, E. Hadjudis, T. Dziembowska, I.M. Mavridis, Keto forms of salicylaldehyde schiff bases: structural and theoretical aspects, J. Phy. Chem. B 110 (47) (2006) 23701–23709, https://doi.org/10.1021/jp064110p.
[9] B. Kołodziej, P.M. Dominiak, A. Kościelecka, W. Schilf, E. Grech, K. Woźniak, Neutral and ionic multiple hydrogen bonded moieties in crystal structure of a one tripodal Schiff base, J. Mol. Str. 691 (1–3) (2004) 133–139, https://doi.org/10.1016/j.molstruc.2003.11.040.
[10] W. Schilf, B. Kamieński, A. Szady-Chełmieniecka, E. Grech, A. Makal, K. Woźniak, NMR and X-ray studies of 2, 6-bis (alkylimino) phenol Schiff bases, J. Mol. Str. 844 (2007) 94–101, https://doi.org/10.1016/j.molstruc.2007.05.029.
[11] Y. Sui, X. Zeng, X. Fang, X. Fu, Y. Xiao, L. Chen, M. Li, S. Cheng, Syntheses, structure, redox and catalytic epoxidation properties of dioxomolybdenum (VI) complexes with Schiff base ligands derived from tris (hydroxymethyl) amino methane, J. Mol. Cat. A: Chemical 270 (1–2) (2007) 61–67, https://doi.org/10.1016/j.molcata.2007.01.032.

[12] P.V. Rao, C.P. Rao, A. Sreedhara, E.K. Wegelus, K. Rissanen, E. Kolehmainen, Synthesis, structure and reactivity of trans-$UO_2^{2+}$ complexes of OH-containing ligands: J, Chem. Soc, Dal. Trans. 7 (2000) 1213–1218, https://doi.org/10.1039/B000142M.

[13] W.A. Bubb, H.A. Berthon, P.W. Kuchel, Tris buffer reactivity with low-molecular-weight aldehydes: NMR characterization of the reactions of glyceraldehyde-3-phosphate, Bioorg. Chem. 23 (2) (1995) 119–130, https://doi.org/10.1006/bioo.1995.1010.

[14] Re Roberta, N. Pellegrini, A. Proteggente, A. Pannala, M. Yang, C. Rice- Evans, Antioxidant activity applying an improved ABTS radical cation decolorization assay, Free Radical Biol. Med. 26 (9–10) (1999) 1231–1237, https://doi.org/10.1016/S0891-5849(98)00315-3.

[15] Bruker, APEX2 and SAINT, Brucker AXS Inc., Madison, Wisconsion, USA, 2012.

[16] G.M. Sheldrick, SHELXT – integrated space-group and crystal-structure determination, Acta Cryst. Section A 71 (Pt1) (2015) 3–8, https://doi.org/10.1107/S2053273314026370.

[17] G.M. Sheldrick, Crystal structure refinement with SHELXL, Acta Cryst. Section C71 (Pt 1) (2015) 3–8, https://doi.org/10.1107/S2053229614024218.

[18] C.F. Macrae, I. Sovago, S.J. Cottrell, P.T.A. Galek, P. McCabe, E. Pidcock, M. Platings, G.P. Shields, J.S. Stevens, M. Towler, P.A. Wood, Mercury 4.0: from visualisation to analysis, design and prediction, J. Appl. Cryst. 53 (2020) 226–235, https://doi.org/10.1107/S1600576719014092.

[19] A.L. Spek, check CIF validation ALERTS: what they mean and how to respond, Acta Cryst. E76 (2020) 1–11, https://doi.org/10.1107/S2056989019016244.

[20] M.A. Spackman, D. Jayatilaka, Hirshfeld surface analysis, Cryst. Eng. Comm. 11 (2009) 19–32, https://doi.org/10.1039/B818330A.

[21] J.J. McKinnon, D. Jayatilaka, M.A. Spackman, Towards quantitative analysis of intermolecular interactions with Hirshfeld surfaces, Chem. Commun. 37 (2007) 3814–3816.

[22] P.R. Spackman, M.J. Turner, J.J. McKinnon, S.K. Wolff, D.J. Grimwood, D. Jayatilaka, M.A. Spackman, J. Appl. Cryst. 54 (2021) 1006–1011. CrystalExplorer21. University of Western Australia, http://hirshfeldsurface.net.

[23] S.L. Tan, M.M. Jotani, E.R.T. Tiekink, Utilizing Hirshfeld surface calculations, non-covalent interaction (NCI) plots and the calculation of interaction energies in the analysis of molecular packing, Acta Cryst. E75 (2019) 308–318, https://doi.org/10.1107/S2056989019001129.

[24] J Da Chai, M Head-Gordon, Long-range corrected hybrid density functionals with damped atom-atom dispersion corrections, Phys. Chem. Chem. Phys. 10 (44) (2008) 6615–6620, https://doi.org/10.1039/b810189b.

[25] J Da Chai, M Head-Gordon, Systematic optimization of long-range corrected hybrid density functionals, J. Chem. Phys. 128 (8) (2008) 084106–084114, https://doi.org/10.1063/1.2834918.

[26] G.A. Petersson, A.-.L. Mohammad A, A complete basis set model chemistry. II. The total energies of open-shell atoms and hydrides of the first-row atoms, J. Chem. Phys. 9 (September 1990) (1991) 6081–6090.

[27] G.A. Petersson, A. Bennett, T.G. Tensfeldt, M.A. Al-Laham, W.A. Shirley, J. Mantzaris, A complete basis set model chemistry. i. the total energies of closed-shell atoms and hydrides of the first-row elements, J. Chem. Phys. 89 (4) (1988) 2193–2218, https://doi.org/10.1063/1.455064.

[28] S. GRIMME, Semiempirical GGA-type density functional constructed with a long-range dispersion correction, J. Comput. Chem. 27 (2006) 1787–1799, https://doi.org/10.1002/jcc.20495.

[29] B. Mennucci, Polarizable continuum model, Wiley Interdiscip. Rev. Comput. Mol. Sci. 2 (2012) 386–404, https://doi.org/10.1002/wcms.1086.

[30] J. Quertinmont, B. Champagne, F. Castet, M. Hidalgo Cardenuto, Explicit versus implicit solvation effects on the first hyperpolarizability of an organic biphotochrome, J. Phys. Chem. A 119 (2015) 5496–5503, https://doi.org/10.1021/acs.jpca.5b00631.

[31] H. Chermette, Chemical reactivity indexes in density functional theory, J. Comput. Chem. 20 (1) (1999) 129–154, https://doi.org/10.1002/(SICI)1096-987X(19990115)20:1<129::AID-JCC13>3.0.CO;2-A.

[32] R.G. Parr, L.V. Szentpály, S. Liu, Electrophilicity index, J. Am. Chem. Soc. 121 (9) (1999) 1922–1924, https://doi.org/10.1021/ja983494x.

[33] M. Galván, A. Vela, J.L. Gázquez, Chemical reactivity in spin-polarized density functional theory, J. Phys. Chem. 92 (22) (1988) 6470–6474, https://doi.org/10.1021/j100333a056.

[34] F. Méndez, J.L. Gázquez, Chemical reactivity of enolate ions : the local hard and soft acids and bases principle viewpoint, J. Am. Chem. Soc. 116 (1994) 9298–9301, https://doi.org/10.1021/ja00099a055.

[35] L. Meneses, W. Tiznado, R. Contreras, P. Fuentealba, A proposal for a new local hardness as selectivity index, Chem. Phys. Lett. 383 (2004) 181–187, https://doi.org/10.1016/j.cplett.2003.11.019.

[36] P.K. Chattaraj, B. Maiti, U. Sarkar, Philicity: a unified treatment of chemical reactivity and selectivity pratim, J. Phys. Chem. A 107 (25) (2003) 4973–4975, https://doi.org/10.1021/jp034707u.

[37] C. Morell, A. Toro-labbe, New dual descriptor for chemical reactivity, J. Phys. Chem. A 109 (2005) 205–212, https://doi.org/10.1021/jp046577a.

[38] R.K. Roy, S. Krishnamurti, P. Geerlings, S. Pal, Local softness and hardness based reactivity descriptors for predicting intra- and intermolecular reactivity sequences: carbonyl compounds, J. Phys. Chem. A 102 (1998) 3746–3755, https://doi.org/10.1021/jp973450v.

[39] M.S. Blois, Antioxidant determinations by the use of a stable free radical, Nature 181 (4617) (1958) 1199–1200, https://doi.org/10.1038/1811199a0.

[40] A. Szydłowska-Czerniak, C. Dianoczki, K. Recseg, G. Karlovits, E. Szłyk, Determination of antioxidant capacities of vegetable oils by ferric-ion spectrophotometric methods, Talanta 76 (4) (2008) 899–905, https://doi.org/10.1016/j.talanta.2008.04.055.

[41] M. Özyürek, N. Güngör, S. Baki, K. Güçlü, R. Apak, Development of a silver nanoparticle-based method for the antioxidant capacity measurement of polyphenols, Anal. Chem. 84 (18) (2012) 8052–8059, https://doi.org/10.1021/ac301925b.

[42] M. Oyaizu, Antioxidative activities of products of browning reaction prepared from glucosamine, Jap. J. Nut. Diet. 44 (6) (1986) 307–315, https://doi.org/10.5264/eiyogakuzashi.44.307.

[43] G.M. Morris, R. Huey, A.J. Olson, UNIT using AutoDock for ligand-receptor docking. Current Protocols in Bioinformatics, 2008, https://doi.org/10.1002/0471250953.bi0814s24.

[44] https://www.rcsb.org/structure/2Y9X.

[45] E.C. Meng, T.E. Ferrin, UCSF Chimera - a visualization system for exploratory research and analysis, J. Comput. Chem. 25 (13) (2004) 1605–1612, https://doi.org/10.1002/jcc.20084.

[46] E.F. Pettersen, T.D. Goddard, C.C. Huang, G.S. Couch, D.M. Greenblatt, E.C. Meng, T.E. Ferrin, UCSF Chimera - a visualization system for exploratory research and analysis, J. Comput. Chem. 25 (13) (2004) 1605–1612, https://doi.org/10.1002/jcc.20084.

[47] M.J. Turner, J.J. Mackinnon, S.K. Wolff, D.J. Spackman, P.R. Jayatilaka, D.M. A. Spackman, Crystal Explorer17.5, University of Western Australia, Perth, 2017.

[48] M.M. Solomon, S.A. Umoren, M.A. Quraishi, M. Salman, Myristic acid based imidazoline derivative as effective corrosion inhibitor for steel in 15% HCl medium, J. Coll. Inter. Sci. 551 (2019) 47–60, https://doi.org/10.1016/j.jcis.2019.05.004.

[49] M.M. Solomon, S.A. Umoren, In-situ preparation, characterization and anticorrosion property of polypropylene glycol/silver nanoparticles composite for mild steel corrosion in acid solution, J. Coll. Inter. Sci. 462 (2016) 29–41, https://doi.org/10.1016/j.jcis.2015.09.057.

[50] H. Gerengi, H.I. Ugras, M.M. Solomon, S.A. Umoren, M. Kurty, N. Atar, Synergistic corrosion inhibition effect of 1-ethyl-1-methylpyrrolidinium tetrafluoroborate and iodide ions for low carbon steel in HCl solution, J. Adh. Sci. Tech. 30 (21) (2016) 2383–2403, https://doi.org/10.1080/01694243.2016.1183407.

[51] G. Kear, B. Barker, F.C. Walsh, Electrochemical corrosion of unalloyed copper in chloride media—a critical review, Corr. Sci. 46 (1) (2004) 109–135, https://doi.org/10.1016/S0010-938X(02)00257-3.

[52] Dq. Zhang, Lx. Gao, Gd. Zhou, Inhibition of copper corrosion by bis-(1-benzotriazolymethylene)-(2, 5-thiadiazoly)-disulfide in chloride media, App. Sur. Sci. 225 (1–4) (2004) 287–293, https://doi.org/10.1016/j.apsusc.2003.10.016.

[53] K. Khaled, M.N. Hamed, K. Abdel-Azim, N. Abdelshafi, Inhibition of copper corrosion in 3.5% NaCl solutions by a new pyrimidine derivative: electrochemical and computer simulation techniques, J. Sol. St. Electr. 15 (4) (2011) 663–673, https://doi.org/10.1007/s10008-010-1110-0.

[54] M.M. Antonijević, S.M. Milić, M.B. Petrović, Films formed on copper surface in chloride media in the presence of azoles Petrović, Corros. Sci. 51 (6) (2009) 1228–1237, https://doi.org/10.1016/j.corsci.2009.03.026.

[55] S.S. Abd ElRehim, H.H. Hassan, M.A. Amin, Corrosion inhibition study of pure Al and some of its alloys in 1.0M HCl solution by impedance technique, Corros. Sci. 46 (1) (2004) 5–25, https://doi.org/10.1016/S0010-938X(03)00133-1.

[56] Y. Xu, S. Zhang, W. Li, et al., Experimental and theoretical investigations of some pyrazolo-pyrimidine derivatives as corrosion inhibitors on copper in sulfuric acid solution, App. Sur. Sci. 459 (2018) 612–620, https://doi.org/10.1016/j.apsusc.2018.08.037.

[57] M.M. Lebrini, M. Lagrenee, H. Vezin, et al., Experimental and theoretical study for corrosion inhibition of mild steel in normal hydrochloric acid solution by some new macrocyclic polyether compounds, Corr. Sci. 49 (5) (2007) 2254–2269, https://doi.org/10.1016/j.corsci.2006.10.029.

[58] N. Kumari, P. Kumari Paul, L. Gope, J. Adhes, et al., Studies on anticorrosive action of synthesized indolines on mild steel in 15% HCl solution, J. Adh. Sci. Tech. 31 (14) (2017) 1524–1544, https://doi.org/10.1080/01694243.2016.1263473.

[59] M. Kissi, M. Bouklah, B. Hammouti, et al., Establishment of equivalent circuits from electrochemical impedance spectroscopy study of corrosion inhibition of steel by pyrazine in sulphuric acidic solution, App. Sur. Sci. 252 (12) (2006) 4190–4197, https://doi.org/10.1016/j.apsusc.2005.06.035.

[60] T. Zhang, W. Jiang, H. Wang, S. Zhang, Synthesis and localized inhibition behaviour of new triazine-methionine corrosion inhibitor in 1 M HCl for 2024-T3 aluminium alloy, Mater. Chem. Phys. (237) (2019), 121866, https://doi.org/10.1016/j.matchemphys.2019.121866.

[61] B. Sakki, M.E. Said, B. Mezhoud, et al., Experimental and theoretical study on corrosion inhibition of pyridinium salts derivatives for API 5L Gr. B steel in acidic media, J. Adhes. Sci. Technol. 36 (20) (2022) 2245–2268, https://doi.org/10.1080/01694243.2021.2008193.

[62] D.S. Chauhan, K. Ansari, A.A. Sorour, et al., Thiosemicarbazide and thiocarbohydrazide functionalized chitosan as ecofriendly corrosion inhibitors for carbon steel in hydrochloric acid solution, Int. J. Bio. Mac. 107 (2018) 1747–1757, https://doi.org/10.1016/j.ijbiomac.2017.10.050.

[63] P. Singh, E.E. Ebenso, L.O. Olasunkanmi, et al., Electrochemical, theoretical, and surface morphological studies of corrosion inhibition effect of green naphthyridine derivatives on mild steel in hydrochloric acid, J. Phy. Chem. C 120 (6) (2016) 3408–3419, https://doi.org/10.1021/acs.jpcc.5b11901.

[64] L.R. Domingo, M.J. Aurell, P. Pérez, R. Contreras, Quantitative characterization of the global electrophilicity power of common diene/dienophile pairs in Diels-Alder reactions, Tetrahedron 58 (22) (2002) 4417–4423, https://doi.org/10.1016/S0040-4020(02)00410-6.

[65] D. Hannachi, N.E.H. Amrane, L. Merzoud, H. Chermette, Exploring the antioxidant activity of thiaflavan compounds : a quantum chemical study, New. J. Chem. 45 (2021) 13451–13462, https://doi.org/10.1039/D1NJ01996A.
[66] S. Alaoui. Mrani, E. Ech-chihbi N. Arrousse, Z. Rais, F. El Hajjaji, C. El Abiad, S. Radi, J. Mabrouki, M. Taleb & S. Jodeh. DFT and electrochemical investigations on the corrosion inhibition of mild steel by novel Schiff 's base derivatives in 1M HCl solution. Arab. J. Sci. Eng. 46 52021). 5691–5707. https://doi.org/10.1007/s13369-020-05229-4.
[67] H.B. Michaelson, The work function of the elements and its periodicity the work function of the elements and its periodicity, J. Appl. Phys. 48 (1977) 4729, https://doi.org/10.1063/1.323539.
[68] A. Lesar, I. Milošev, Density functional study of the corrosion inhibition properties of 1, 2, 4-triazole and its amino derivatives, Chem. Phys. Lett. 483 (2009) 198–203, https://doi.org/10.1016/j.cplett.2009.10.082.
[69] N. Kerru, L. Gummidi, S.V.H.S. Bhaskaruni, S.N. Maddila, P. Singh, S. B. Jonnalagadda, A comparison between observed and DFT calculations on structure of 5-(4-chlorophenyl)-2-amino-1,3,4-thiadiazole, Sci. Rep. 9 (2019) 1–17, https://doi.org/10.1038/s41598-019-55793-5.
[70] M.A. Roselan, N. Zakaria, N.H. Faujan, et al., In vitro cytotoxicity assay, mushroom tyrosinase inhibitory activity and release analysis of kojic monooleate nanodelivery system and in silico molecular docking study against 2Y9X target enzyme, J. Drug. Del. Sci. Tech. 66 (2021), 102764, https://doi.org/10.1016/j.jddst.2021.102764.
[71] A. Soroceanu, A. Bargan, Advanced and biomedical applications of Schiff-base ligands and their metal complexes: a review, Crystals 12 (10) (2022) 1436, https://doi.org/10.3390/cryst12101436.
[72] A.A. Abdel Aziz, A.N.M. Salem, M.A. Sayed, M.M. Abdaly, Synthesis, structural characterization, thermal studies, catalytic efficiency and antimicrobial activity of some M (II) complexes with ONO tridentate Schiff base N-salicylidene-o-aminophenol (saphH2), J. Mol. Str. 1010 (2012) 130–138, https://doi.org/10.1016/j.molstruc.2011.11.043.
[73] G. Saravanan, P. Pannerselvam, C. Prakash, Synthesis and anti-microbial screening of novel schiff bases of 3-amino-2-methyl quinazolin 4-(3H)-one, J. Adv. Pharm. Tech. Res. 1 (3) (2010) 320, https://doi.org/10.4103/0110-5558.72426.
[74] Ö. Güngör, P. Gürkan, Synthesis and characterization of higher amino acid Schiff bases, as monosodium salts and neutral forms. Investigation of the intramolecular hydrogen bonding in all Schiff bases, antibacterial and antifungal activities of neutral forms, J. Mol. Str. 1074 (2014) 62–70, https://doi.org/10.1016/j.molstruc.2014.05.032.
[75] K.S. Kumar, S. Ganguly, R. Veerasamy, E. De Clercq, Synthesis, antiviral activity and cytotoxicity evaluation of Schiff bases of some 2-phenyl quinazoline-4 (3) H-ones, Eur. J. Med Chem. 45 (11) (2010) 5474–5479, https://doi.org/10.1016/j.ejmech.2010.07.058.
[76] D. Sriram, P. Yogeeswari, N.S. Myneedu, V. Saraswat, Abacavir prodrugs: microwave-assisted synthesis and their evaluation of anti-HIV activities, Bioor. Med. Chem. Lett. 16 (8) (2006) 2127–2129, https://doi.org/10.1016/j.bmcl.2006.01.050.
[77] G. Hu, G. Wang, N. Duan, X. Wen, T. Cao, S. Xie, et al., Design, synthesis and antitumor activities of fluoroquinolone C-3 heterocycles (IV): s-triazole Schiff–Mannich bases derived from ofloxacin, Acta Pharm. Sinica B 2 (3) (2012) 312–317, https://doi.org/10.1016/j.apsb.2011.11.003.
[78] N. El-wakiel, M. El-keiy, M. Gaber, Synthesis, spectral, antitumor, antioxidant and antimicrobial studies on Cu (II), Ni (II) and Co (II) complexes of 4- [(1H-Benzoimidazol-2-ylimino)-methyl]-benzene-1, 3-diol, Spectr. Acta Part A: Mol. Biom. Spectr. 147 (2015) 117–123, https://doi.org/10.1016/j.saa.2015.03.020.
[79] E. Pontiki, D. Hadjipavlou-Litina, A.T. Chaviara, Evaluation of anti-inflammatory and antioxidant activities of copper (II) Schiff mono-base and copper (II) Schiff base coordination compounds of dien with heterocyclic aldehydes and 2-amino-5-methyl-thiazole, J. Enzy. Inhib. Med. Chem. 23 (6) (2008) 1011–1017, https://doi.org/10.1080/14756360701841251.
[80] S.M. Bensaber, H.A. Allafe, N.B. Ermeli, S.B. Mohamed, A.A. Zetrini, S.G. Alsabri, et al., Chemical synthesis, molecular modelling, and evaluation of anticancer activity of some pyrazol-3-one Schiff base derivatives, Med. Chem. Res. 23 (12) (2014) 5120–5134, https://doi.org/10.1007/s00044-014-1064-3.
[81] S.B. Desai, P.B. Desai, K.R. Desai, Synthesis of some Schiff bases, thiazolidinones and azetidinones derived from 2, 6-diaminobenzo [1, 2-d: 4, 5-d'] bisthiazole and their anticancer activities, Heter. Comm. 7 (1) (2001) 83–90, https://doi.org/10.1515/HC.2001.7.1.83.
[82] P. Przybylski, A. Huczynski, K. Pyta, B. Brzezinski, F. Bartl, Biological properties of Schiff bases and azo derivatives of phenols, Curr. Org. Chem. 13 (2) (2009) 124–148, https://doi.org/10.2174/138527209787193774.
[83] I. Król-Starzomska, A. Filarowski, M. Rospenk, A. Koll, S. Melikova, Proton transfer equilibria in Schiff bases with steric repulsion, J. Phys. Chem. A 108 (11) (2004) 2131–2138, https://doi.org/10.1021/jp035009c.
[84] M.E. Bluhm, M. Ciesielski, H. Görls, O. Walter, M. Döring, Complexes of schiff bases and intermediates in the copper-catalyzed oxidative heterocyclization by atmospheric oxygen§, Inorg. Chem. 42 (26) (2003) 8878–8885, https://doi.org/10.1021/ic034773a.
[85] L. Wang, W. Qin, X. Tang, W. Dou, W. Liu, Q. Teng, et al., A selective, cell-permeable fluorescent probe for $Al^{3+}$ in living cells, Org. Biom. Chem. 8 (16) (2010) 3751–3757, https://doi.org/10.1039/C0OB00123F.
[86] E. Raczuk, B. Dmochowska, J. Samaszko-Fiertek, J. Madaj, Different Schiff bases—structure, Importance Classif. Mol. 27 (3) (2022) 787, https://doi.org/10.3390/molecules27030787.
[87] V. Velezheva, P. Brennan, P. Ivanov, A. Kornienko, S. Lyubimov, K. Kazarian, et al., Synthesis and antituberculosis activity of indole–pyridine derived hydrazides, hydrazide–hydrazones, and thiosemicarbazones, Bioor. Med. Chem. Lett. 26 (3) (2016) 978–985, https://doi.org/10.1016/j.bmcl.2015.12.049.